View metadata, citation and similar papers at core.ac.uk
brought to you by CORE
provided by CERN Document Server

Astronomy & Astrophysics manuscript no. cs-hh
June 15, 2006
© ESO 2006

arXiv:astro-ph/0605716 v2 14 Jun 2006

Low sulfur depletion in the Horsehead PDR⋆

J.R. Goicoechea[1], J. Pety[1,2], M. Gerin[1], D. Teyssier[3], E. Roueff[4], P. Hily-Blant[2], and S. Baek[1]

[1] LERMA–LRA, UMR 8112, CNRS, Observatoire de Paris and Ecole Normale Supérieure, 24 Rue Lhomond, 75231 Paris cedex 05, France.
e-mail: javier@lra.ens.fr, gerin@lra.ens.fr
[2] IRAM, 300 rue de la Piscine, 38406 Grenoble cedex, France.
e-mail: pety@iram.fr,hilyblan@iram.fr
[3] European Space Astronomy Centre, Urb. Villafranca del Castillo, P.O. Box 50727, Madrid 28080, Spain.
e-mail: dteyssier@sciops.esa.int
[4] LUTH UMR 8102, CNRS and Observatoire de Paris, Place J. Janssen 92195 Meudon cedex, France.
e-mail: evelyne.roueff@obspm.fr

Received 2006 March 24; accepted 2006 June 9

ABSTRACT

Aims. We present 3.65″ × 3.34″ angular–resolution IRAM *Plateau de Bure Interferometer* (PdBI) observations of the CS J=2–1 line toward the Horsehead *Photodissociation Region* (PDR), complemented with IRAM–30m single–dish observations of several rotational lines of CS, $C^{34}S$ and HCS^+. We analyse the CS and HCS^+ photochemistry, excitation and radiative transfer to obtain their abundances and the physical conditions prevailing in the cloud edge. Since the CS abundance scales to that of sulfur, we determine the gas phase sulfur abundance in the PDR, an interesting intermediate medium between translucent clouds (where sulfur remains in the gas phase) and dark clouds (where large depletions have been invoked).

Methods. A nonlocal non–LTE radiative transfer code including dust and cosmic background illumination adapted to the Horsehead geometry has been developed to carefuly analyse the CS, $C^{34}S$, HCS^+ and $C^{18}O$ rotational line emission. We use this model to consistently link the line observations with photochemical models to determine the $CS/HCS^+/S/S^+$ structure of the PDR.

Results. Densities of $n(H_2) \simeq (0.5 - 1.0)\times10^5$ cm^{-3} are required to reproduce the CS and $C^{34}S$ J=2–1 and 3–2 line emission. CS J=5–4 lines show narrower line widths than the CS low–J lines and require higher density gas components not resolved by the ∼10″ IRAM–30m beam. These values are larger than previous estimates based in CO observations. We found $\chi(CS)=(7\pm3)\times10^{-9}$ and $\chi(HCS^+)=(4\pm2)\times10^{-11}$ as the averaged abundances in the PDR. According to photochemical models, the gas phase sulfur abundance required to reproduce these values is $S/H=(3.5\pm1.5)\times10^{-6}$, only a factor $\lesssim$4 less abundant than the solar sulfur elemental abundance. Since only lower limits to the gas temperature are constrained, even lower sulfur depletion values are possible if the gas is significantly warmer.

Conclusions. The combination of CS, $C^{34}S$ and HCS^+ observations together with the inclusion of the most recent CS collisional and chemical rates in our models implies that sulfur depletion invoked to account for CS and HCS^+ abundances is much smaller than in previous studies.

Key words. Astrochemistry – ISM clouds – molecules – individual object (Horsehead nebula) – radiative transfer – radio lines: ISM

1. Introduction

Sulfur is an abundant element (the solar photosphere abundance is $S/H=1.38\times10^{-5}$; Asplund et al. 2005), which remains undepleted in diffuse interstellar gas (e.g. Howk et al. 2006) and HII regions (e.g. Martín-Hernández et al. 2002; García–Rojas et al. 2006 and references therein) but it is historically assumed to deplete on grains in higher density molecular clouds by factors as large as ∼10^3 (Tieftrunk et al. 1994). This conclusion is simply reached by adding up the observed gas phase abundances of S–bearing molecules in well known dark clouds such as TMC1 (e.g. Irvine et al. 1985; Ohishi & Kaifu 1998). As sulfur is easily ionized (ionization potential ∼10.36 eV), sulfur ions are probably the dominant gas–phase sulfur species in translucent gas. Ruffle et al. (1999) proposed that if dust grains are typically negatively charged, S^+ may freeze–out onto dust grains during cloud collapse more efficiently than neutral species such as oxygen. However, the nature of sulphur on dust grains (either in mantles or cores) is not obvious. Van der Tak et al. (2003) observed large abundances of gas phase OCS, ∼10^{-8}, in star forming regions, and suggested that together with the detection of solid OCS (with an abundance of ∼10^{-7}; Palumbo et al. 1997), it implies that OCS is a major sulfur carrier in dust grains. However, the ∼4.9 μm ice feature attributed to OCS is best reproduced when OCS is mixed with methanol. In fact, the

Send offprint requests to: e-mail: javier@lra.ens.fr

⋆ Based on observations obtained with the IRAM Plateau de Bure interferometer and 30 m telescope. IRAM is supported by INSU/CNRS (France), MPG (Germany), and IGN (Spain).

band is blended with a methanol overtone whose contribution has not been studied in detail (Dartois 2005). In any case, the absence of strong IR features due to S–bearing ices in many ISO's mid–IR spectra (e.g. Boogert et al. 2000; Gibb et al. 2004) and the presence of S II recombination lines in dark clouds such as Rho Ophiuchi (Pankonin & Walmsley 1978) all argue against a large depletion of sulfur from the gas phase. In this case, the abundance of species such as CS may indicate that something important is lacking from chemical models or that an abundant sulfur–bearing carrier has been missed. Therefore, the abundances of sulfur species remain interesting puzzles for interstellar chemistry. In the case of dense clouds, standard chemical models predict that most of the gas phase sulfur is shared between S, SO and CS (Millar & Herbst 1990), while H_2S is also abundant in the Orion Bar PDR (Jansen et al. 1995). In all these cases, a large sulfur depletion, $\sim 10^2$, was required in the models to explain the observed abundances.

PDRs offer an ideal intermediate medium between diffuse and dark cloud gas to investigate the sulfur depletion problem. In this work we have tried to determine the CS abundance in the Horsehead PDR as a tool for estimating the sulfur gas phase abundance. However, CS chemistry is an open issue itself in different environments, from hot cores (e.g. Wakelam et al. 2004) to extragalactic sources (e.g. Martín et al. 2005). Recent laboratory experiments on dissociative recombination of HCS^+ and OCS^+ (Montaigne et al. 2005) imply a substantial modification of previous reaction rate coefficients, dissociative channels and branching ratios used in chemical models. The latest available reaction rates and collisional coefficients have been used in our photochemical and radiative transfer models.

1.1. The Horsehead nebula

The Horsehead nebula, appears as a dark patch of $\sim 5'$ diameter against the bright HII region IC434. Emission from gas and dust associated with this globule has been detected from IR to millimeter wavelengths (Abergel et al. 2002, Abergel et al. 2003, Pound et al. 2003, Teyssier et al. 2004, Habart et al. 2005, Pety et al. 2005a), although the first astronomical plates were taken ~120 yr ago. In particular, the Horsehead western edge is a PDR viewed nearly edge-on and illuminated by the O9.5V star σOri at a projected distance of ~ 3.5 pc (Anthony-Twarog 1982). The intensity of the incident FUV radiation field is $\chi \simeq 60$ relative to the interstellar radiation field (ISRF) in Draine's units (Draine 1978).

According to the evolutionary view of Reipurth & Bouchet (1984), the Horsehead nebula was a quiescent and dense cloud core embedded in a more diffuse cloud (L1630). The erosive action of the UV radiation from σOri on the ambient gas led to the apparent emergence of the core cloud, as in the earliest stages of Bok globules still attached to their parental cloud. However, the observed morphology together with the velocity gradients of the cloud, require a more involved description including a pre–existing rotating velocity field as well as density inhomogeneities in the initial structures (Pound et al. 2003; Hily–Blant et al. 2005). The erosive effect of the ionizing and dissociating radiation field together with these initial conditions explain the peculiar shaping of the Horsehead nebula. In particular, the densest regions of the initial inhomogeneities are now believed to be the East-West filamentary material connecting it to the parental cloud, and the PDR. In this work we have studied the PDR through CS, $C^{34}S$ and HCS^+ observations.

Table 2. Line parameters for the IRAM 30-m CS observations.

Molecule	Transition	Frequency (GHz)	HPBW (arcsec)
CS	J=2–1	97.980968	25
	J=3–2	146.96905	16
	J=5–4	244.93561	10
$C^{34}S$	J=2–1	96.412982	25
	J=3–2	144.61715	16
HCS^+	J=2–1	85.347884	29

2. Observations and data reduction

2.1. Observations

2.1.1. Pico Veleta single–dish

The single-dish data presented in this paper have been gathered between February and October 2004 at the IRAM 30-m telescope. The Horsehead nebula PDR was mapped in the CS J=2–1 and 5–4 lines in order to provide the short-spacings for the interferometric observations presented thereafter. The final map consists of 5 on-the-fly coverages performed along perpendicular scanning directions, and combined with the PLAIT algorithm introduced by Emerson & Gräve (1988), allowing to efficiently reduce the stripes over the map. The noise levels (1σ rms) per regridded pixel and resolution channel of 80 kHz are of the order of 0.15 K at 3 mm, and 0.64 K at 1.3 mm. The latter value was not low enough to provide any useful mapping information at 1.3 mm since the CS J=5–4 line peak is $\lesssim$1 K.

In complement to these data, dedicated positions were probed over a larger set of species and transitions. The frequency switching mode was used to observe CS J=2–1, 3–2 and 5–4 lines, as well as $C^{34}S$ J=2–1, 3–2, and HCS^+ J=2–1 lines. Table 2 summarizes the corresponding observing parameters. Longer integrations allowed to reach, in a resolution channel of 40 kHz, rms noise levels of 25, 42 and 36 mK at 3, 2, and 1.3 mm respectively. All CS and $C^{34}S$ lines were detected with a S/N ratio better than 10. Figs. 4 and 8 show some spectra collected at positions inside and across the PDR.

The data were first calibrated to the T_A^* scale using the so-called chopper wheel method (Penzias & Burrus 1973), and finally converted to main beam temperatures using efficiencies (B_{eff}/F_{eff}) of 0.81, 0.74 and 0.50 at 3, 2 and 1.3 mm respectively.

2.1.2. Plateau de Bure Interferometer

PdBI observations dedicated to this project were carried out with 6 antennae in the BCD configuration (baseline lengths from 24 to 331 m) from August 2004 to March 2005. The

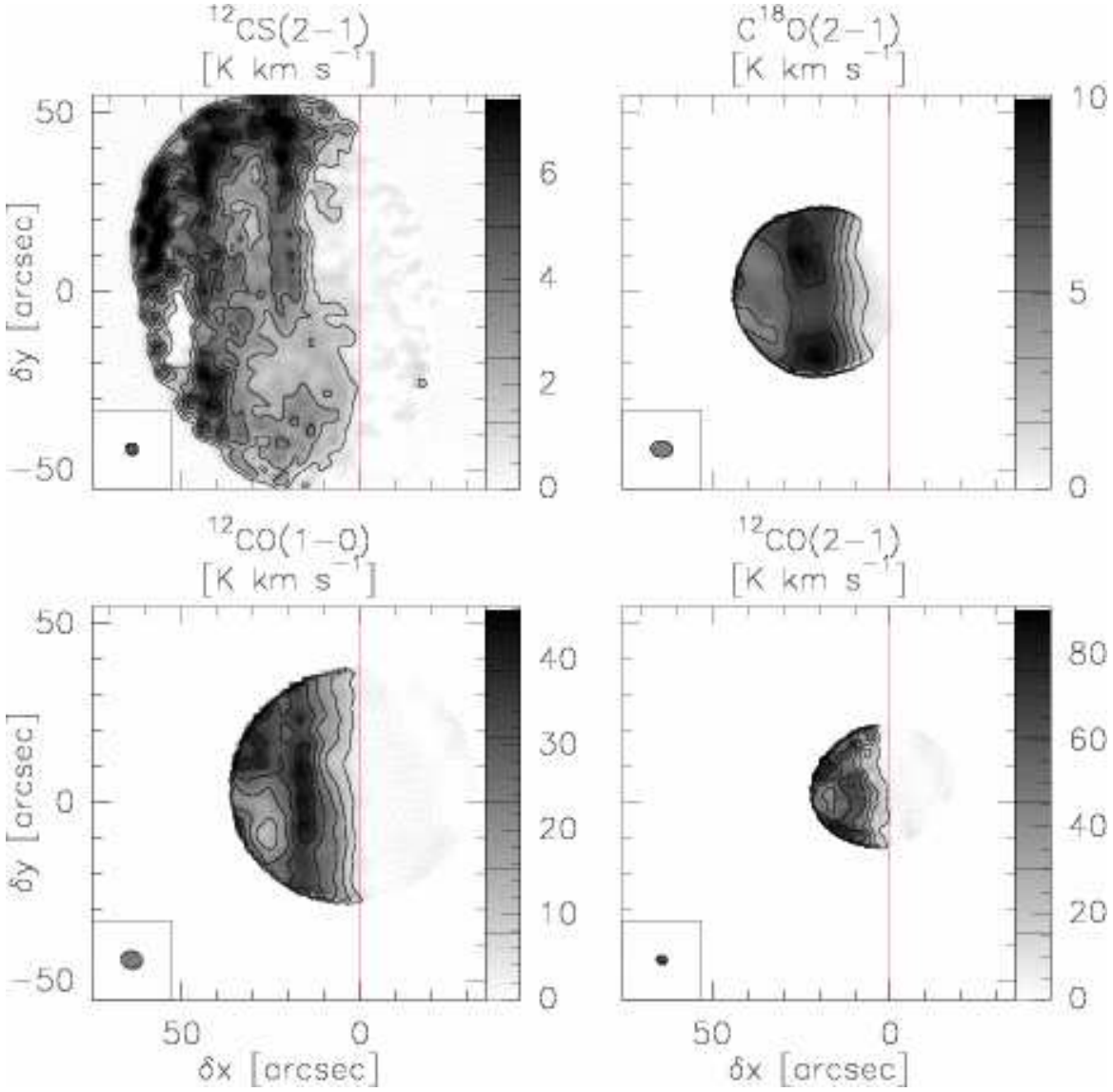

Fig. 1. Integrated emission maps obtained with the Plateau de Bure Interferometer. The center of all maps has been set to the mosaic phase center: RA(2000) = 05h40m54.27s, Dec(2000) = -02°28'00″. The map size is 110″ × 110″, with ticks drawn every 10″. The synthesized beam is plotted in the bottom left corner. The emission of all lines is integrated between 10.1 and 11.1 km s^{-1}. Values of contour level are shown on each image wedge. The four panels are shown in a coordinate system adapted to the source: *i.e.* maps have been rotated by 14° counter–clockwise around the image center to bring the exciting star direction in the horizontal direction as this eases the comparison of the PDR models. Maps have also been horizontally shifted by 20″ to set the horizontal zero at the PDR edge, delineated by the vertical line.

580 MHz instantaneous IF–bandwidth allowed us to simultaneously observe CS, l-C_3H and ^{34}SO at 3 mm using 3 different 20 MHz–wide correlator windows. Another window was centered on the ^{13}CO J=2–1 line frequency at 1 mm. The full IF bandwidth was also covered by continuum windows both at 3.4 and 1.4 mm. Only CS J=2–1 and ^{13}CO J=2–1 (not shown here) were detected.

We observed a seven–field mosaic. The mosaic was Nyquist sampled in declination at 3.4 mm and Nyquist sampled in Right Ascension at 1.3 mm. This ensures correct sampling in the illuminating star direction both at 3 and 1 mm while maximizing the field of view along the edge of the PDR eases the deconvolution. This mosaic, centered on the IR peak (Abergel et al. 2003), was observed for about 30 hours of *telescope* time with 6 antennas. This leads to an *on–source* integration time of useful data of 10 hours after filtering out data with tracking errors larger than 1″ and with phase noise worse than 40° at 3.4 mm. The rms phase noises were between 15 and 40° at 3.4 mm, which introduced position errors < 0.5″. Typical 3.4 mm raw resolution was 2.5″.

Table 1. Observation parameters.

	Phase center		Number of fields
Mosaic 1	$\alpha_{2000} = 05^h40^m54.27^s$	$\delta_{2000} = -02°28'00''$	7
Mosaic 2	$\alpha_{2000} = 05^h40^m53.00^s$	$\delta_{2000} = -02°28'00''$	4

Molecule & Line	Frequency (GHz)	Beam (arcsec)	PA (°)	Noise[a] ($K\,km\,s^{-1}$)	Obs. date
Mosaic 1					
^{12}CS J=2–1	97.981	3.65×3.34	48	1.2×10^{-1}	Aug. & Oct. 2004 and Mar. 2005
$C^{18}O$ J=2–1	219.560	6.54×4.31	65	9.8×10^{-2}	Mar. 2003
Mosaic 2					
^{12}CO J=1–0	115.271	5.95×5.00	65	1.2×10^{-1}	Nov. 1999
^{12}CO J=2–1	230.538	2.97×2.47	66	1.7×10^{-1}	Nov. 1999

[a] The noise values quoted here are the noises at the mosaic center (Mosaic noise is inhomogeneous due to primary beam correction; it steeply increases at the mosaic edges). Those noise values have been computed in 1 $km\,s^{-1}$ velocity bin.

Table 3. Calibrator fluxes in Jy.

Date	B0420−014		B0607−157	
	3 mm	1 mm	3 mm	1 mm
20.08.2004	3.4	2.9	1.4	0.93
04.10.2004	3.4	2.9	1.6	0.90
27.02.2005	3.5	2.9	1.6	0.90
02.03.2005	3.2	2.3	1.6	0.89
12.03.2005	3.2	2.3	1.6	0.90
13.03.2005	3.2	2.3	1.6	1.00

2.2. Data processing

All data reduction was done with the GILDAS[1] softwares supported at IRAM (Pety 2005b). Standard calibration methods using nearby calibrators were applied to all the PdBI data. The calibrator fluxes used for the absolute flux calibration are summarized in Table 3.

Following Gueth et al. 1996, single–dish, fully sampled maps obtained with the IRAM-30m telescope (see section 2.1.1) were used to produce the short–spacing visibilities filtered out by each mm-interferometer (*e.g.* spatial frequencies between 0 and 15 m for PdBI). Those pseudo-visibilities were merged with the observed, interferometric ones. For imaging, we followed the method described by Pety et al. (2005) to produce images in different lines of the same source. This results in inhomogeneous noise. In particular, the noise strongly increases near the edges of the field of view. To limit this effect, the mosaic field–of–view is truncated.

Moreover, the natural synthesized beam ($3.58'' \times 1.89''$ at PA 37°) is very asymmetric due to the low declination of the Horsehead nebula. We chooe to taper the weights of the *uv* visibilities before imaging using a Gaussian of size 400 m×115 m at PA 80° to obtain an almost circular clean beam ($3.65'' \times 3.34''$ at PA 48°). This considerably eased the deconvolution as 1) the larger beam increases the brightness sensitivity and 2) the secondary sidelobes of the dirty beam are much less patchy. Deconvolved image nevertheless still shows low–level, fake, patchy structures at the scale of the clean beam, mainly along the vertical direction. This is a known artifact of the Högbom CLEAN algorithm when a large spatial dynamic (field–of–view/resolution $\sim 110/3.5 = 30$) is combined with high enough signal–to–noise ratio.

[1] See http://www.iram.fr/IRAMFR/GILDAS for more information about the GILDAS software.

Table 4. IRAM–30m line observation parameters from Gaussian fits.

Molecule/ Transition	Offset ($''$)	Δv_{FWHM} ($km\,s^{-1}$)	$\int T_A^* dv$ ($K\,km\,s^{-1}$)
CS J=2–1	-52,-40	0.75±0.01	2.60±0.01
	-64,+30	0.89±0.01	3.63±0.01
	-35,-25	0.78±0.01	3.68±0.01
	-20,-15	0.77±0.01	3.55±0.01
CS J=3–2	-52,-40	0.72±0.01	1.82±0.02
	-64,+30	0.93±0.01	2.58±0.02
	-35,-25	0.76±0.01	2.73±0.02
	-20,-15	0.80±0.01	2.40±0.02
CS J=5–4	-52,-40	0.43±0.02	0.35±0.01
	-64,+30	0.76±0.02	0.62±0.02
	-35,-25	0.58±0.02	0.52±0.01
	-20,-15	0.60±0.03	0.40±0.02
$C^{34}S$ J=2–1	-52,-40	0.47±0.02	0.26±0.01
	-64,+30	0.67±0.04	0.38±0.02
	-35,-25	0.59±0.02	0.40±0.01
	-20,-15	0.58±0.03	0.45±0.02
$C^{34}S$ J=3–2	-52,-40	0.48±0.04	0.20±0.01
	-64,+30	0.74±0.05	0.28±0.02
HCS^+ J=2–1	-52,-40	0.8±0.3	0.07±0.03
	-35,-25	0.6±0.3	0.05±0.03
	-20,-15	0.9±0.4	0.10±0.03

3. Results

The PdBI integrated emission map of the CS J=2–1 line, complemented with previous maps of CO J=1–0, 2–1 and $C^{18}O$ J=2–1 lines (Pety et al. 2005a), is shown in Fig. 1. Integrated emission profiles for these lines and for the small hydrocarbon c–C_3H_2 2_{12}–1_{01} line emission and 1.2 mm continuum emission (Pety et al. 2005a) are shown in Fig. 2. In Fig. 1 the four panels are shown in a coordinate system adapted to the source: *i.e.*

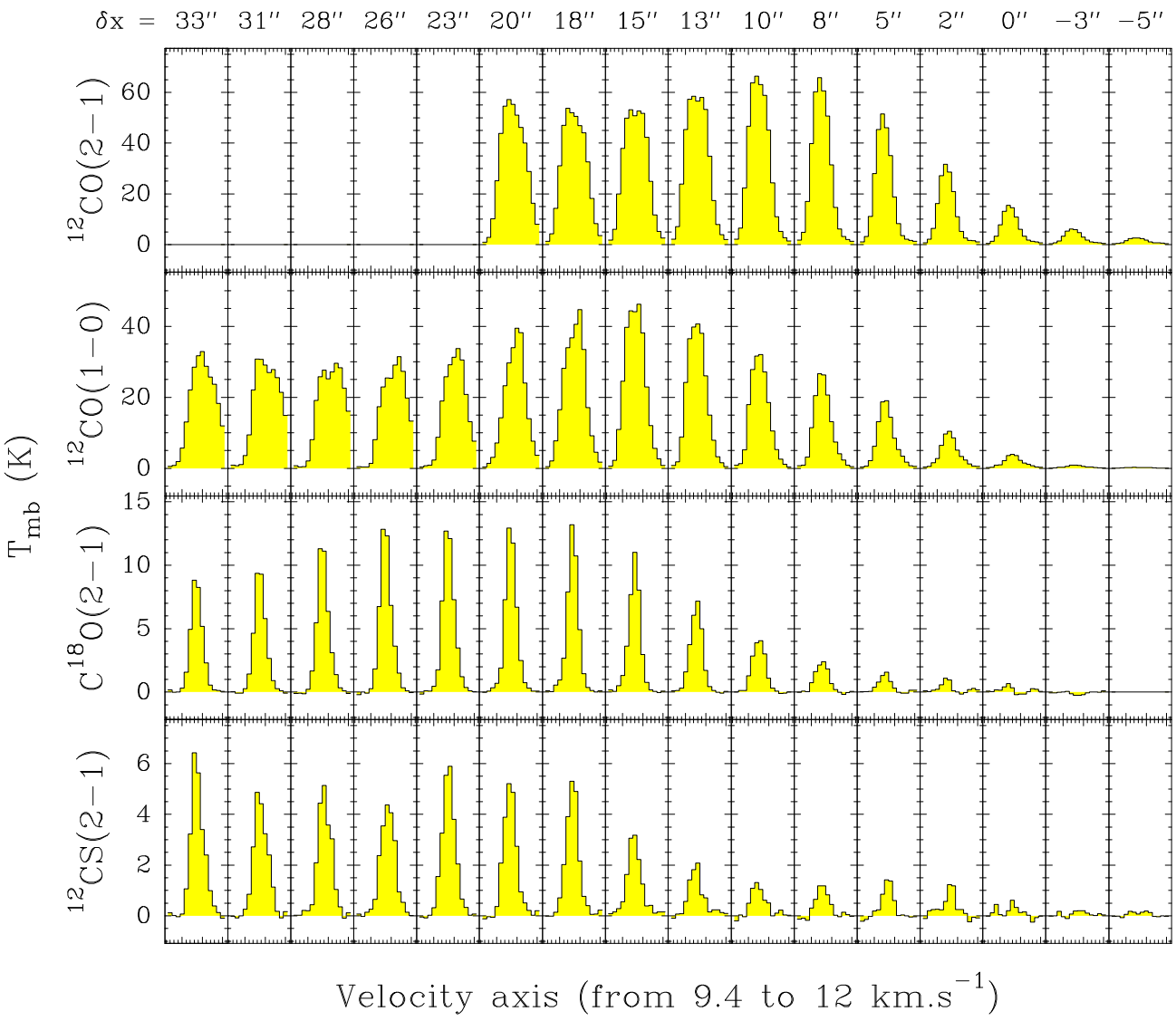

Fig. 3. Spectra along the direction of the exciting star at $\delta y = 0''$. ^{12}CO J=1–0, C^{18}O J=2–1 and ^{12}CS J=2–1 spectra cubes were smoothed by a 15″–FWHM 1D–Gaussian along the y direction perpendicular to the illuminating star direction. Due to their small field of view (in particular in the y direction), the ^{12}CO J=2–1 data were just smoothed by a 5″–FWHM circular Gaussian.

maps have been rotated by 14° counter–clockwise around the image center to bring the exciting star direction in the horizontal direction as this eases the comparison with edge–on PDR models. Maps have also been horizontally shifted by 20″ to the east in order to set the horizontal zero at the PDR edge (delineated by the vertical line). Therefore, the coordinate system is converted from δRA to δx and from δDEC to δy in arcsec (see Fig. 1). In the following, our spatial scale to interpret the PdBI maps will refer to the δx scale.

PdBI observations show that the CS emission is strikingly different from that of other species observed at comparable spatial resolutions. CS does not follow the filamentary pattern along the cloud edge revealed by mid–IR (Abergel et al. 2003), H_2 (Habart et al. 2005) or CCH and c-C_3H_2 emission (Pety et al. 2005a). Instead, the behavior of the CS J=2–1 line emission is more similar to that of CO and shows a steep rise across the PDR and a plateau in the shielded region. Besides, the CS J=2–1 line emission peak occurs in the well-shielded regions and does not coincide with the C^{18}O J=2–1 nor with the 1.2 mm continuum peaks (i.e. the temperature weighted density peaks, see Fig. 2). Therefore, PdBI observations suggests that CS is more abundant in the lower density regions and/or it shows line opacity effects in the denser regions. These results confirm that there are differences in the spatial distribution of small hydrocarbons (Pety et al. 2005a) and other species with similar excitation requirements. PdBI CO, C^{18}O and CS line spectra along the direction of the exciting star ($\delta y = 0''$) are shown in Fig. 3. The CS J=2–1 emission peak and line widths are comparable to those of C^{18}O J=2–1. Nevertheless, the CS emission distribution profile in the δx direction is less smooth, which can be an artifact of the data reduction and/or related to the CS photochemistry. The CS emission increases like the C^{18}O emission in the PDR edge but in the shielded gas, CS rises when C^{18}O decreases. On the other hand, ^{12}CO peaks closer to the PDR edge and lines have broader line widths (Pety et al. 2005a) indicative of their much larger opacities.

CS and $C^{34}S$ single–dish observations at larger spatial scales are presented in Fig. 4. CS line ratios are similar in all observed PDR positions. However, there is a trend for CS lines to peak where $C^{18}O$ emission decreases. Again, this is indicative of larger abundances in the lower density regions and/or line opacity effects in the denser regions. The latter hypothesis is playing a role because CS J=3–2 lines show asymmetrical profiles in the whole region, especially red–wing like self–absorptions. See for example the (−52, −40) position with respect to the IRAM–30m $C^{18}O$ J=2–1 map of Hily–Blant et al. (2005; Fig. 4). In addition, CS J=3–2 and 2–1 lines must be optically thick since their intensity is only a factor ∼5 stronger than the analogous $C^{34}S$ lines, significantly lower than the $^{32}S/^{34}S$=23 solar isotopic ratio (Bogey et al. 1981). In addition, CS $\frac{3-2}{2-1}$ line ratios are ∼0.7 while the optically thin $C^{34}S$ $\frac{3-2}{2-1}$ line ratios are larger ∼0.9. Therefore, the CS J=3–2 line is likely to be the most opaque CS line. Finally, Fig. 8 shows clear detections of the HCS^+ J=2–1 line. As the expected HCS^+ abundance is lower than that of $C^{34}S$, these lines are weak and should be optically thin. Line intensities are quite similar in all observed PDR positions.

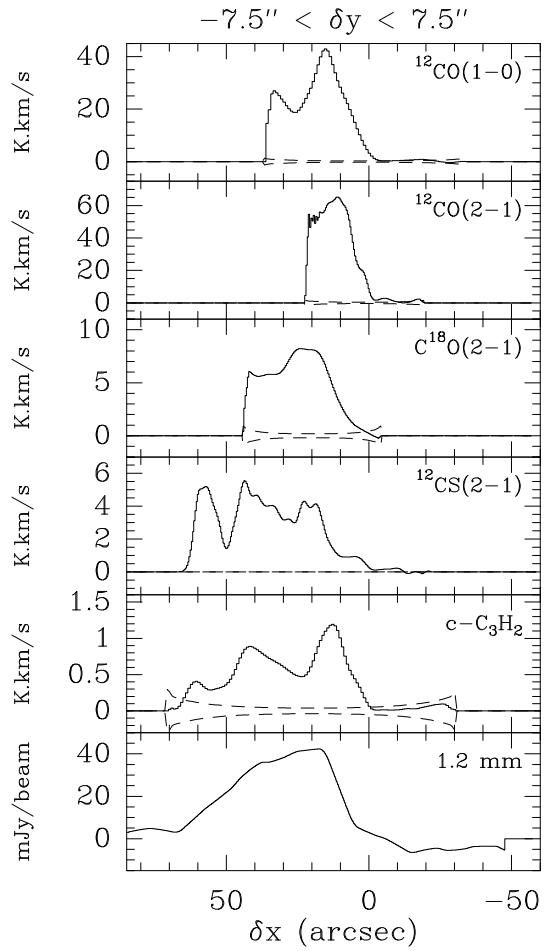

Fig. 2. Emission profiles along the exciting star direction (PA = -104° in the equatorial coordinate system). To improve the signal–to–noise ratio, emission profiles have been integrated along the perpendicular direction between $-7.5'' < \delta y < +7.5''$. We show from top to bottom ^{12}CO J=2–1, ^{12}CO J=1–0, $C^{18}O$ J=2–1, ^{12}CS J=2–1, c–C_3H_2 2_{12}–1_{01} and 1.2 mm dust continuum emission (Pety et al. 2005a). The 3σ noise level is indicated by the dashed lines. It rises at the cut edges due to the primary beam correction. Note that the fields of view of the ^{12}CO and $C^{18}O$ data are smaller than the field of view of the ^{12}CS data because of the smaller mosaic size and/or the higher frequency.

Table 5. Einstein coefficients, transition upper level energies and critical densities for the range of temperatures considered in this work.

Molecule	Transition	A_{ij} (s^{-1})	E_i (K)	n_{cr} (cm^{-3})
$C^{18}O$	J=2–1	6.01×10^{-7}	15.8	$\sim8\times10^3$
HCS^+	J=2–1	1.11×10^{-5}	6.1	$\sim5\times10^4$
$C^{34}S$	J=2–1	1.60×10^{-5}	6.9	$\sim4\times10^5$
	J=3–2	5.79×10^{-5}	13.9	$\sim1\times10^6$
CS	J=2–1	1.68×10^{-5}	7.1	$\sim4\times10^5$
	J=3–2	6.07×10^{-5}	14.1	$\sim1\times10^6$
	J=5–4	2.98×10^{-4}	35.3	$\sim5\times10^6$

4. Numerical methodology

4.1. Photochemical models

We have used the *Meudon PDR code* (publicly available at **http://aristote.obspm.fr/MIS/**), a photochemical model of a unidimensional stationary PDR (Le Bourlot et al. 1993). The model has been described in detail elsewhere (Le Petit et al. 2006). In few words, the PDR code solves the FUV radiative transfer in an absorbing and diffusing medium of gas and dust. This allows the explicit computation of the FUV radiation field (continuum+lines) and therefore, the explicit integration of consistent C and S photoionization rates together with H_2, CO, ^{13}CO, and $C^{18}O$ photodissociation rates. Penetration of FUV radiation into the cloud strongly depends on dust properties through dust absorption and scattering of FUV photons. Properties of dust grains are those described in Pety et al. (2005). We have taken a single dust albedo coefficient of 0.42 and an scattering asymmetry parameter of 0.6.

Once the FUV field has been determined, the steady-state chemical abundances are computed for a given chemical network. The *Ohio State University (osu)* gas–phase chemical network (osu.2005; September 2005 release; **http://www.physics.ohio-state.edu/~eric/research.html**) has been used as our chemical framework. The most important changes compared to previous versions are the decrease, by a factor of 2, of rate coefficients of photoionization and photodissociation reactions produced by cosmic–ray–induced H_2 secondary photons, the inclusion of fluorine (F) and its chemistry (see Neufeld et al. 2005) and the update of several reaction rates. In addition, several changes have been carried out by us on the chemical network. In particular, we have introduced different ^{18}O bearing species into the chemical network by assuming similar reaction rates to those involving the major isotopologues. Fractionation reactions have been added follow-

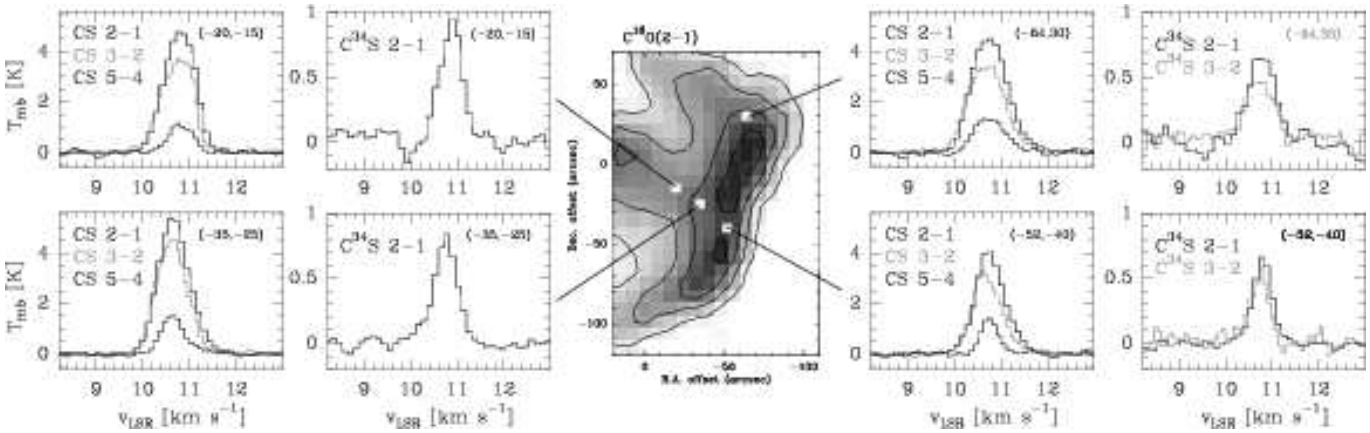

Fig. 4. IRAM–30m CS J=2–1, 3–2 and 5–4, and $C^{34}S$ J=2–1 and 3–2 single–dish observations (histograms) at different positions of the Horsehead PDR single–dish $C^{18}O$ J=2–1 emission centered at $\alpha_{2000} = 05^h40^m58^s$, $\delta_{2000} = -02°27'20''$ (from Hily–Blant et al. 2005).

ing Graedel et al. (1982) and specific photodissociation cross–sections for $C^{18}O$ are explicitly introduced to compute the corresponding photodissociation rate. When available, we have also used the photodissociation rates given by van Dishoeck (1988), which are explicitly calculated for the Draine interstellar radiation field (ISRF). Finally, we have further upgraded the sulfur network by adding the most recent reaction rates, dissociation channels and branching ratios of HCS^+ and OCS^+ dissociative recombination (Montaigne et al. 2005) and by including the CS photoionization (ionization potential ~11 eV). These processes have direct impact on CS chemistry. The resulting network involves ~450 species and ~5000 reactions. Finally, the model computes the thermal structure of the PDR by solving the balance between the most important processes heating and cooling the gas (see Le Bourlot et al. 1993). Our *standard conditions* for the model of the Horsehead PDR include a power–law density profile (Eq. 2) and a FUV radiation field enhanced by a factor $\chi = 60$ with respect to the Draine ISRF (see table 6). Different sulfur gas phase abundances, S/H, have been investigated. To be consistent with PdBI CO observations, thermal balance was solved until the gas temperature reached a minimum value of 30 K, then a constant temperature was assumed.

Table 6. Horsehead standard conditions and gas phase abundances.

Parameter	Value
Radiation field χ	60 (Draine units)
Cosmic ray ionization rate ζ	$5 \times 10^{-17} s^{-1}$
Density profile $n_H = n(H) + 2n(H_2)$	50 to 2×10^5 cm^{-3}
Line of sight spatial depth l_{depth}	0.05–0.1 pc
Line of sight inclination angle φ	0^o to 5^o
He/H=$n(He)/n_H$	1.00×10^{-1}
O/H	3.02×10^{-4}
C/H	1.38×10^{-4}
N/H	7.95×10^{-5}
^{18}O/H	6.04×10^{-7}
Cl/H	1.00×10^{-7}
Si/H	1.73×10^{-8}
Mg/H	1.00×10^{-8}
F/H	6.68×10^{-9}
Na/H	2.30×10^{-9}
Fe/H	1.70×10^{-9}
P/H	9.33×10^{-10}

4.2. Radiative transfer models

We have used a simple nonlocal non–LTE radiative transfer code to model our millimeter line observations. The code handles spherical and plane-parallel geometries and accounts for line trapping, collisional excitation, and radiative excitation by absorption of microwave cosmic background and dust continuum photons. Arbitrary density, temperature or abundance profiles, and complex velocity gradients can be included. A more detailed description is given in the Appendix. The choice of a nonlocal treatment is needed to analyze optically thick lines of abundant, high–dipole moment molecules, such as CS, in regions where the gas density is below the critical densities of the associated transitions. Table 5 shows the critical densities of observed $C^{18}O$, HCS^+ and CS lines. Under these conditions, radiative transfer and opacity effects may dominate the line profile formation. Our radiative transfer analysis has been used to infer abundances and physical conditions directly from observations but also to predict line spectra from the photochemical model results. The following temperature dependent collisional rate coefficients[2] have been adopted:

– for CS: we have used the latest CS + He collisional rates from Lique et al. (2006), kindly provided by F. Lique prior to publication, scaled by the reduced mass factor $(\mu_{CS-H_2}/\mu_{CS-He})^{1/2}$. Most of the models were repeated with the older collisional rates of Turner et al. (1992).

[2] Some of them retrieved from BASECOL, a data base for collisional excitation data at `http://www.amdpo.obspm.fr/basecol`. We considered H_2, He and H as the collisional partners in all CS, $C^{34}S$, HCS^+ and $C^{18}O$ excitation models. See Appendix.

– for $C^{34}S$: same as CS but using $C^{34}S$ spectroscopy to compute collisional excitation rates through detailed balance.
– for $C^{18}O$: CO + H_2 de–excitation rates from Flower (2001) but using $C^{18}O$ spectroscopy to compute collisional excitation rates through detailed balance.
– for HCS^+: HCS^+ + He collisional rates from Monteiro (1984), scaled by the reduced mass factor $(\mu_{HCS^+-H_2}/\mu_{HCS^+-He})^{1/2}$, have been used.

5. Modeling and interpretation

5.1. CS, $C^{34}S$ and HCS^+ single–dish emission

In order to get a first order approximation of the CS excitation and column density, we have assumed that level populations are only determined by a Boltzmann distribution at a single rotational temperature. If one accepts that lines are optically thin, this approach corresponds to the widely used rotational–diagram. However, observed CS/$C^{34}S$ intensity ratios, and CS line profiles (see Fig. 4) clearly show that the low–J CS lines are optically thick towards the Horsehead. Therefore, we have included optical depth effects and built a rotational–diagram corrected for opacity through:

$$ln\,\frac{N_i^{thin}}{g_i} + ln\,C_\tau = ln\,N - ln\,Q - \frac{E_i}{T_{rot}} \quad (1)$$

where N_i^{thin} are the upper level populations determined from observations in the optically thin limit (underestimated if lines are optically thick), E_i is the upper i-level energy in K, Q is the partition function at T_{rot} and C_τ is the line opacity correction factor $\frac{\tau_{ij}}{1-e^{-\tau_{ij}}}$ >1 (Goldsmith & Langer 1999). We have performed this analysis at different cloud positions. Resulting diagrams are shown in Fig. 5 as a function of different CS J=2–1 line opacities (τ_{2-1} = 0, 1 and 5). In the optically thin limit CS column densities are $N(CS)$ ~5×10^{13} cm^{-2} and they have to be considered as lower limits. Low excitation temperatures (T_{rot} ~6-9 K) are also inferred from the rotational–diagrams. These values, much lower than expected gas temperatures in a PDR, are suggestive of radiative excitation effects in CS lines and level populations far from thermalization. Therefore, we only use the rotational–diagrams as input for the first iteration of a more complex analysis.

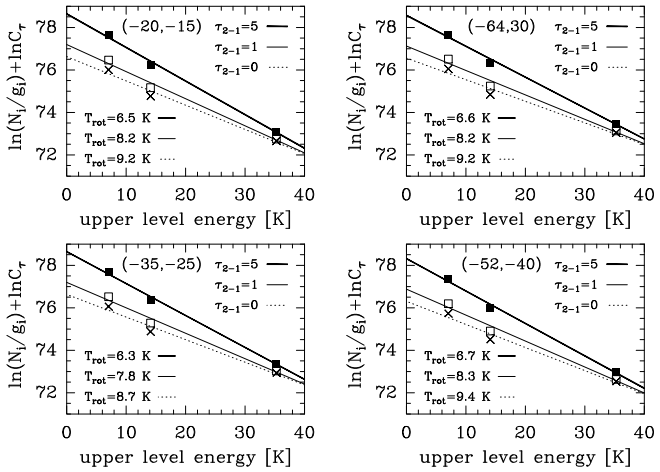

Fig. 5. CS rotational–diagrams corrected for line opacity effects at each observed position of Fig.4. Rotational–diagrams for different considered CS J=2–1 line opacities (τ_{2-1}) are shown in each box. Rotation temperatures for each opacity correction are also indicated.

In order to obtain a more detailed overview of the CS excitation, we have made several statistical equilibrium calculations (see Appendix) around the expected physical conditions in the Horsehead. In particular, we have run a grid of single–component models for T_k=10, 20, 30, 50 and 70 K, $n(H_2)$=10^4, 5×10^4, 10^5 and 5×10^5 cm^{-3}, and $\chi(CS)$ from 10^{-10} to 10^{-7}. As a reference value, the cloud total extinction is assumed to be constant and equal to A_V=20 mag in all models, i.e. the spatial length is changed accordingly. Fig. 6 specifically shows selected results for T_k=30 K, which gives appropriate absolute intensities for the CS lines. In particular, integrated line intensity ratios of observed lines as a function of CS abundance for different densities are shown. Averaged ratios from CS single–dish observations are $\frac{3-2}{2-1}$ ~0.7, $\frac{5-4}{2-1}$~0.2 and $\frac{5-4}{3-2}$~0.3. Therefore, densities ≥5×10^4 cm^{-3} are needed to populate the CS intermediate–J levels. On the other hand, for high densities (≥5×10^5 cm^{-3}), collisions start to efficiently populate these levels and the predicted line ratios involving the CS J=5–4 line become much larger than observed. Thus, mean densities are in the range $n(H_2)$ ≃(0.5–1.0)$\times10^5$ cm^{-3}, i.e. lower than CS critical densities (table 5). Excitation temperatures are predicted to be subthermal, T_{ex} <T_k, especially for the highest frequency lines. Due to line–trapping, the maximum T_{ex} is reached at the center of the cloud, while it graduately drops at both surfaces where line photons are optically thin and line trapping is not efficient. The only exception is the CS J=1–0 transition which shows an increase of the excitation temperature, T_{ex}^{1-0}, at both surfaces. This rising in T_{ex}^{1-0} is due to the significant collisional excitation coupling from the J=0 to J=2 level, and to the large radiative de–excitation rates from J=2 to J=1 level. At both surfaces, where optically thin CS J=2–1 line photons can easily escape from the cloud (T_{ex}^{2-1} decreases), the above excitation conditions favor the population of the J=1 level with respect to the J=0 level. Therefore, T_{ex}^{1-0} can reach large suprathermal values. A typical example is shown in Fig. A.2. Thus, within this range of parameters and even if physical conditions are homogeneous, excitation gradients must be taken into account.

For these temperatures and densities, T_k ≃20–30 K and $n(H_2)$ ≃(0.5–1.0)$\times10^5$ cm^{-3}, the CS $\frac{5-4}{2-1}$ and $\frac{5-4}{3-2}$ line ratios are better fitted in the interval $\chi(CS)$ ≃(0.2-1.0)$\times10^{-8}$. Nevertheless, the $\frac{3-2}{2-1}$ line ratio is systematically predicted to be larger than observed in these single–component models. Therefore, a more complex density structure and/or additional opacity effects in low–J CS lines may be affecting the observed profiles. The latter hypothesis is clearly favored by the fact that the $C^{34}S$ $\frac{3-2}{2-1}$ line intensity ratio is larger (~0.9) than the CS $\frac{3-2}{2-1}$ ratio (~0.7) and thus closer to the single–component model predictions. Since the $C^{34}S$ emission is optically thin, radiative transfer effects are less important and $C^{34}S$ column densities can be accurately determined.

Table 7. One-component radiative transfer model parameters.

Parameter	Value
T_k	20–25 K
$n(H_2)$	(7–12)×10^4 cm^{-3}
v_{turb}	0.3–0.5 km s^{-1}
$\chi(C^{34}S)$	(3±1)×10^{-10}
$\chi(HCS^+)$	(4±2)×10^{-11}

Table 8. Two–component radiative transfer model parameters.

Parameter	Value
T_k	20–25 K
$n(H_2)$	(3–7)×10^4 cm^{-3}
dense component	(2–6)×10^5 cm^{-3}
(filling factor)	0.3
v_{turb}	0.3–0.4 km s^{-1}
dense component	0.2–0.3 km s^{-1}
$\chi(CS)$	(7±3)×10^{-9}
S/H	(3.5±1.5)×10^{-6}

$C^{34}S$ single–component radiative transfer models for selected positions within the region have been run (Fig. 7). Since $C^{34}S$ emission can arise from different gas components of higher density, not resolved by the large single–dish beam, we have modeled each position in spherical geometry. This allows to explore different components of different beam filling factors. The maximum extinction in the models varies from A_V=20 to 12 mag depending on the cloud position. These values are consistent with those obtained from single–dish 1.2 mm dust continuum emission observations (Teyssier et al., 2004, Pety et al. 2005a). Following our previous general excitation calculations we have considered gas temperatures in the range 20–25 K. For these conditions, densities between $n(H_2)$=7×10^4 and 1.2×10^5 cm^{-3} satisfactorily reproduce the observed $C^{34}S$ absolute intensities. Best fits are obtained for turbulence velocities (see Appendix for the definition of v_{turb}) between 0.3 and 0.4 km s^{-1} (Table 7). Although $C^{34}S$ is slightly enhanced where $C^{18}O$ decreases, we have averaged the 4 positions to find the mean $C^{34}S$ abundance in the region covered with single–dish observations and found $\chi(C^{34}S)$=(3±1)×10^{-10}. Since nucleosynthesis models favor a constant galactic $^{32}S/^{34}S$ ratio and many observations reproduce the solar ratio within their error bars (Wannier et al. 1980 ; Frerking et al. 1980), especially in local diffuse clouds (Lucas & Liszt, 1998), we adopt $^{32}S/^{34}S$=23 here as the isotopic ratio in the Horsehead. Therefore, the derived $\chi(C^{34}S)$ abundance translates to $\chi(CS)$=(7±3)×10^{-9}. The same physical conditions at each position have been used to model the HCS^+ J=2–1 lines (see Fig. 8). Lines are reproduced for an averaged abundance of $\chi(HCS^+)$=(4±2)×10^{-11}, therefore, a CS/HCS^+ ≃175 abundance ratio is derived.

Using the CS abundance inferred from the $C^{34}S$ analysis, we have now tried to fit the CS lines at each position. Since a single–component model does not reproduce the observed line ratios and absolute intensities, we have explored other possibilities. In principle, CS low–J lines are optically thick and may not trace the high density gas revealed by $C^{34}S$, especially if the medium is inhomogeneous and dense clumps and a more diffuse interclump medium coexist. The same argumentation has been used to interpret HCN and $H^{13}CN$ observations in the Orion Bar PDR (Lis & Schilke, 2003). In addition, it is well known that low–J CS lines may not be a good column density tracer if their emission is scattered by a low density halo (González-Alfonso & Cernicharo 1993). This process can be a common effect in optically thick lines of high–dipole moment molecules such as CS or HCO^+ (Cernicharo & Guélin 1987). In this scenario, the CS J=3–2 and 2–1 lines from the dense medium will be attenuated and scattered over larger areas than the true spatial extend of the dense clumps. This possibility has been analyzed in more detail in the next section. Fortunately, observations of the CS J=5–4 line allow to directly trace the dense clumps more safely (Table 8). In particular, we found that these lines can only be reproduced with denser gas components, $n(H_2)$= (4±2)×10^5 cm^{-3}, not resolved by the ∼10″ beam of the IRAM–30m telescope at ∼250 GHz. Note that the CS J=5–4 line widths are fitted if the turbulent velocity in the denser gas is ∼0.2 km s^{-1}, a factor 2 lower than the one required by the $C^{34}S$ J=3–2 and 2–1 lines (Fig. 7). Thus, a different spatial origin for this line emission is favored.

At this stage we have a general knowledge of the CS and HCS^+ excitation and abundance in the region. In the following sections we concentrate in the photochemistry of these species. Only higher angular observations provide the appropriate linear scale to resolve the most important physical gradients in the PDR edge. Hence, interferometric observations should allow a better comparison with chemical predictions.

5.2. The PDR edge

PdBI $C^{12}O$ J=2–1, 1–0, $C^{18}O$ J=2–1, and CS J=2–1 observations along the direction of the exciting star (at δy= 0″) are shown in Fig. 3. Here we take these spectra as representative of the PDR edge and try to constrain its physical conditions through a combined analysis of photochemical and radiative transfer models. Both models use a unidimensional plane–parallel description of the geometry. Although some physical processes require more complex geometries, the main physical and chemical gradients across the illuminated direction can be consistently described in this way. Plane–parallel geometry was judged to be the best approach for this edge–on PDR since H_2 and PAH emissions are only observed at the illuminated edge and not deeper inside the cloud (Habart et al. 2005).

In this analysis, we have used the PdBI CS J=2–1 and $C^{18}O$ J=2–1 lines. As low–J ^{12}CO optical depths are very high, they do not trace the bulk of material. The intensity peak of these lines only provide a good estimation of the CO excitation temperatures (i.e. a lower limit to the gas temperature). Since the asymptotic brightness temperature of CO J=1–0 lines is ∼30 K, we take this value as the minimum of T_k in the PDR. We note that lower temperatures do not reproduce the observed line intensities. For the rest of the (warmer) positions closer to the PDR edge, the gas temperature was determined by solv-

ing the thermal balance. The predicted gas temperature in the density peak is ∼50 K while it rises to ∼200–250 K in the H_2 emitting regions where the density is $n_H \simeq 10^3$-10^4 cm^{-3}. More exact temperature values require observations of higher–J CO lines at comparable spatial resolution. We are currently analysing ^{13}CO J=3–2 data from the SMA interferometer.

Regarding the density structure, both the observed H_2 and PAH mid–IR emission, together with their spatial segregation, are much better reproduced with a steep density gradient than with an uniform density (Habart et al. 2005). The same density gradient is needed to correctly reproduce the observed offset between the small hydrocarbons (Pety et al. 2005a) and H_2 emission (where the density is not at its peak). Therefore, in order to reproduce PdBI observations of CS and C^{18}O, a steep power–law density gradient at the illuminated regions and a step–density in the more shielded region have been assumed.

The following methodology was carried out: a full PDR model with Horsehead *standard conditions* (see section 4.1) was run with a particular choice of the density gradient described in Eq. 2. Afterwards, the PDR output was used as input for the nonlocal radiative transfer calculation in a fashion described in appendix A.2. In this way, physical parameters can be tuned more accurately by iteration of different radiative transfer models. Once better parameters have been found, a new PDR computation is performed with this choice of physical parameters. Hence, the most appropriate physical and chemical description of the PDR edge was found through the *PDR model→transfer model→check with observations→transfer model→PDR model* iterative process. Therefore, synthetic CS and C^{18}O abundance profiles are consistently computed as a function of the edge distance δx (in arcsec) and directly compared with observations.

Different PDR spatial depths were investigated. Depending on the adopted density profile, the spatial depth l_{depth} is determined by the line of sight visual extinction. However, the A_V value depends on the method used to measure it. If optically thin 1.2 mm dust emission is used (Teyssier et al. 2004; Pety et al. 2005a; Habart et al. 2005), the resulting column densities depend on the usually unknown grain properties and on the assumed temperature. Taking into account our poor knowledge of the cloud thermal structure, a factor ∼2 of uncertainty in A_V can be assumed. In addition, the angular resolution of millimeter continuum observations is at least a factor ∼2 worse than PdBI molecular line observations. Due to the steep decrease of the density towards the edge, and due to the ∼11″ beam of 1.2 mm continuum observations, the observed emission peak will appear deeper inside the cloud, shifted a few arcsec from the real density peak (which is closer to the edge). Therefore, together with the PDR edge location, the exact peak density position can also be uncertain by a few arcsec. Finally, beam dilution has to be also taken into account when comparing single–dish versus interferometric observations. Here we have chosen l_{depth} =0.05-0.1 pc, which implies extinction peaks around $A_V \simeq$15-30 magnitudes. These values are expected in compact globules (Reipurth & Bouchet 1984). Since CS and C^{18}O excitation and line transfer are quite different, the following combined analysis provides an accurate description of the edge density structure. The empirical density profile in the models, n_H=$n(H)$+2$n(H_2)$, as a function of δx is:

$$n_H(\delta x) = \begin{cases} n_H(0) + [n_H(\delta x_1) - n_H(0)] \left(\frac{\delta x}{\delta x_1}\right)^{\beta}; \delta x_1 \geq \delta x \geq 0 \\ n_H(\delta x_1); \delta x_2 \geq \delta x > \delta x_1 \\ n_H(\delta x_2); \delta x > \delta x_2 \end{cases} \quad (2)$$

where δx is the distance away from the PDR edge, $n_H(0)$ is the ambient density at the edge, and $n_H(\delta x_1)$ and $n_H(\delta x_2)$ are constant densities in the $\delta x_2 \geq \delta x > \delta x_1$ and $\delta x > \delta x_2$ regions respectively. Selected photochemical models are shown in Fig. 9. The normalized population of the H_2 v=1, J=3 level is shown in the *upper* panel and is used to place the δx–axis origin of the models and thus to accurately check with observations. Although some uncertainty in the location the PDR edge exists, we place the peak of this curve at the maximum of observed H_2 1–0 S(1) 2.12 μm excited line (δx ∼10″; Habart et al. 2005). Best models are found for a peak density around $n_H(\delta x_1)$=2×10^5 cm^{-3}. This density is reached in a length of ∼2.5″–5″ (or 5–10×10^{-3} pc) and stays constant in a length of $\delta x_2 - \delta x_1 \lesssim$20″ (or 0.04 pc). In order to fit the smooth decrease of C^{18}O emission and also of the 1.2 mm continuum emission, the density has to decrease again by at least a factor ∼2. We have simply modeled this as a step-function for δx>δx_2 and decrease the density to $n_H(\delta x_2)$=10^5 cm^{-3}. We have chosen δx_1 = 12″ and δx_2 = 30″. Our models confirm that high density gas and a large gradient slope, β ∼3–4, are needed to reproduce the PdBI and H_2 observations (Habart et al. 2005), although we found a slightly smaller gradient scale length.

As proposed by Habart et al. (2005) the PDR edge can be slightly inclined with respect to the line of sight by a small angle φ. In plane–parallel geometry, the maximum inclination can be estimated assuming that the observed spatial extend of the H_2 emission, d_{H_2}, is mainly due to the projection of l_{depth} in the plane of the sky, thus $sin\,\varphi \simeq d_{H_2}/l_{depth}$. Since d_{H_2} ∼0.01 pc, an inclination angle φ ∼5^o, has been considered in the radiative transfer models (see Appendix A.2). As expected, even such a small inclination shifts the emission peak significantly and should therefore be taken into account. Fig. 10 shows the PdBI C^{18}O line observations and the combined PDR+transfer modeling including such geometrical effects. The agreement is excellent, probably favored by the well–established CO photochemistry (Fig. 9) and because C^{18}O J=2–1 lines do not show complex radiative transfer effects (τ_{2-1} ∼0.8).

To analyse the spatial distribution of the CS abundance predicted by photochemical models at the PDR edge we have also tried to fit the PdBI CS J=2–1 lines. Fig. 9 shows the effects of different sulfur abundances; S/H=2×10^{-5} and S/H=2×10^{-6}. Fig. 11 (no inclination) and Fig. 12 (inclination considered) show the resulting synthetic CS map, using S/H=2×10^{-6} and a minimum gas temperature of 30 K, over PdBI observations at two constant δy cuts (δy=30″ and 0″). Contrary to C^{18}O, the CS emission detected with the PdBI at a fixed δx near the edge shows an emission gradient in the δy direction, e.g. line peaks are brighter as δy increases. As a consequence model predictions fit better the δy=30″ cut than the δy=0″ one. Besides, larger gas phase sulfur abundances are obtained if the bulk of the gas in the PDR edge is warmer, i.e. minimum gas temperatures of ∼100 K (Fig. 9, right panel). This may be an indication

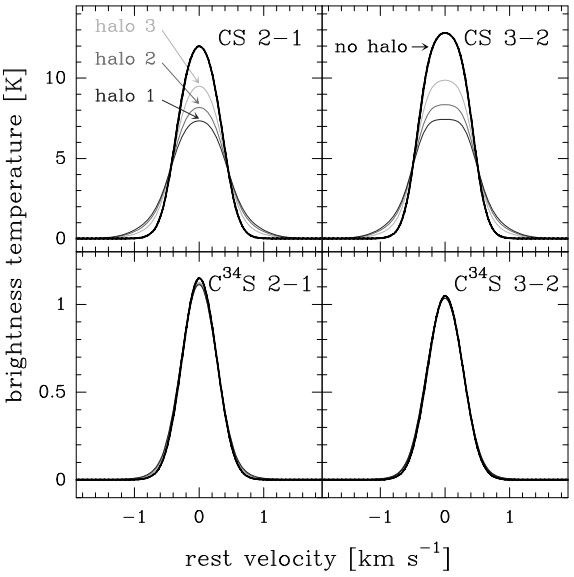

Fig. 13. CS and $C^{34}S$ synthetic line profiles for a cloud with a depth of 0.1 pc, T_k=30 K, $n(H_2)=10^5$ cm^{-3} and $\chi(CS)=7\times10^{-9}$ (thick curves). Thin curves show the resulting spectra if the same cloud is surrounded by different diffuse halos (3: $n(H_2)=5\times10^3$ cm^{-3}, 2: $n(H_2)=8\times10^3$ cm^{-3} and 1: $n(H_2)=1\times10^4$ cm^{-3}). The CS abundance in the cloud is determined more precisely from CS high-J and $C^{34}S$ low–J observations, otherwise it is underestimated. Note that the intensity levels are comparable to those observed in the Horsehead.

of larger temperatures at the cloud edge and lower sulfur depletions. Note that an accurate estimation of the CS abundance at high resolution from a single PdBI line is not straightforward. Such determination requires aperture synthesis observations of additional CS lines to have a minimum idea of the CS excitation in different positions.

In addition, since $C^{34}S$ observations at the same high–angular resolution were not available, we could not estimate additional opacity effects in previous PdBI CS models ($\tau_{2-1} \gtrsim 2$). In the following we have tried to estimate the worse possible scenario affecting the CS lines in the line–of–sight, i.e. the presence of a surrounding low density halo. Of course, the greatest effect can appear in the shielded regions where the gas column density is largest. Therefore we modelled a typical position where CS is well spatially resolved with the following parameters: l_{depth}=0.1 pc, T_k=30 K, $n(H_2)=10^5$ cm^{-3}, v_{turb}=0.35 km s^{-1} and $\chi(CS)=7\times10^{-9}$, (the averaged CS abundance obtained from the detailed CS and $C^{34}S$ excitation analysis of previous section). We consider in addition that a low density halo of diffuse gas with the same χ(CS) surrounds the region. We take T_k=10 K, v_{turb}=0.7 km s^{-1} and densities in the interval $n(H_2)=(5\text{–}10)\times10^3$ cm^{-3}. The same modeling was carried out for $C^{34}S$. Fig. 13 shows model results. As expected, a low density halo efficiently self-absorbs CS line photons in the most opaque lines, i.e. the low–J CS lines. As a result, the observed CS line intensities are attenuated and abundances can be easily underestimated. However, this effect can be different at different positions, since the line opacity also changes. Apart from uncertainties in sulfur chemistry or instrumental effects in interferometric observations, diffuse gas can also contribute to explain differences between models and observations in Figs. 11 and 12. Since, optically thick lines are affected by this effect (Fig.13), only the observation of ^{13}CS or $C^{34}S$ isotopologues can help to provide more accurate abundance determinations. In the following, the CS chemistry is analyzed in more detail.

5.3. CS chemistry and S-abundance

Predicted $C^{18}O/CO/C/C^+$ and $CS/HCS^+/S/S^+$ structures for a unidimensional PDR with Horsehead *standard conditions* are shown in Fig. 9 (see section 4.1). Variation of the sulfur elemental abundance almost does not affect the CO or $C^{18}O$ abundance profiles, but it slightly modifies the predicted C/C^+ abundance profiles because charge transfer reactions between C^+ and S, and between C and S^+ are clearly altered by the sulfur depletion. The following results are of course determined by our present knowledge and uncertainties on S–chemistry, and on reaction rates at different temperatures. According to the latest *ion storage ring* experiments (Montaigne et al. 2005), only 19% of the HCS^+ dissociative recombination results in CS + H while the fracture of the C–S bond dominates the dissociation (81%). Since these experiments can not separate the contribution of the CH + S or SH + C channels in the latter process, we have adopted the same branching ratio (0.405) for both channels. The reaction rate coefficient is $k_{DR}(HCS^+)_{fast}=9.7\times10^{-7}(T/300)^{-0.57}$ cm^3 s^{-1}. We have also included the latest OCS^+ dissociative recombination rates from Montaigne et al. (2005). The CS + O production channel now occurs at a rate 3 times slower than in previous chemical networks. All these modifications clearly influence the amount of CS formed from a given sulfur abundance, and thus the sulfur depletion estimations. Fig. 9 (left panel) also shows the effect of adopting the older HCS^+ and OCS^+ dissociative recombination rates and branching ratios. In particular, $k_{DR}(HCS^+)_{slow}=5.8\times10^{-8}(T/300)^{-0.75}$ cm^3 s^{-1}. However, since $HCS^+ + e^- \rightarrow CS + H$ was the only channel considered and the $OCS^+ + e^- \rightarrow CS + O$ process was faster, smaller sulfur abundances were required to obtain the same CS abundances.

In the most external layers of the cloud, still dominated by the FUV radiation field, CS is predominantly formed by HCS^+ dissociative recombination and principally destroyed by photodissociation and charge transfer with H^+. Once the gas is shielded, OCS^+ dissociative recombination and reaction of C with SO also contributes to CS formation, while its destruction is now governed by ion–molecule reactions, mainly with HCO^+ but also with H_3O^+. These last two reactions with abundant molecular ions return HCS^+ again. The peak abundance of HCS^+ occur at $A_V \lesssim 2$ mag, where it is formed by reaction of CS^+ with H_2 and destroyed by dissociative recombination. For this reason, an order of magnitude change in $k_{DR}(HCS^+)$ clearly modifies its peak abundance in the outer PDR layers. In the more shielded regions, HCS^+ destruction is dominated by dissociative recombination and reaction with atomic oxygen to form HCO^+ and OCS^+. Since the predicted CS abundance scales with S/H, and CS formation is dominated by HCS^+ dis-

sociative recombination, we have used our CS/$C^{34}S$/HCS^+ observations and modeling to estimate S/H.

Fig. 14 shows results of a grid of photochemical models for different sulfur elemental abundances from S/H=10^{-8} to 2×10^{-5}, using the latest HCS^+ and OCS^+ dissociative recombination rates. CS and HCS^+ abundances with respect to H_2 are shown as a function of S/H at two different PDR positions (A_v ~10 and ~2 mag respectively; see Fig. 9). Densities at these positions are the same, $n(H_2)$=10^5 cm^{-3}, but we have taken different PDR positions in order to plot the HCS^+ maximum abundance and to get the CS/HCS^+ ratio closer to observations. Inside the cloud, the predicted maximum HCS^+ abundances are a factor ~3 lower than observed. Horizontal shaded regions mark the CS and HCS^+ abundances derived from observations and radiative transfer modeling. For clarity, HCS^+ abundances have been multiplied by a factor of 1000. Finally, the vertical shaded region shows the estimated sulfur elemental abundance in the Horsehead derived from the overlap region between observed and predicted abundances. We derive S/H ~$(3.5\pm1.5)\times10^{-6}$ as the mean value for the PDR. Note that CS is used for the upper limit and HCS^+ for the lower limit. However, according to the inferred HCS^+ abundance, larger sulfur abundances are still possible.

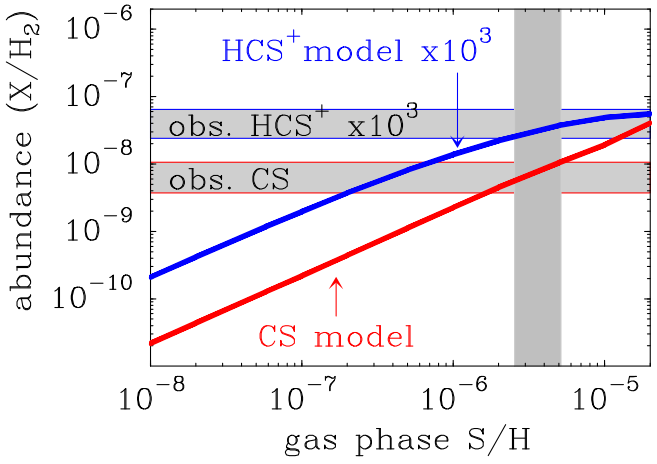

Fig. 14. Photochemical model predictions for the physical and FUV illuminating conditions prevailing in the Horsehead PDR showing the CS and HCS^+ abundance as a function of the sulfur gas phase abundance. Horizontal shaded regions show the CS and HCS^+ abundances derived from the single–dish observations and radiative transfer modeling. Note that for clarity HCS^+ abundances have been multiplied by a factor of 1000. The shaded vertical region shows the estimated sulfur abundance in the Horsehead nebula derived from the constrained fits of CS and HCS^+ abundances.

6. Discussion

Our multi–transition single–dish and aperture synthesis observations and modeling of CS and related species allow us to constrain the sulfur gas phase chemistry in the Horsehead PDR and it also gives some insights on the dense gas properties.

6.1. Densities

The densities found in this work, $n(H_2)$ $\simeq10^5$ cm^{-3}, are larger to those inferred from previous studies based on single–dish CO observations (Abergel et al. 2003; Teyssier et al. 2004). This may be the indication of an inhomogeneous medium characterized by a interclump medium (well traced by CO) and a denser clump medium (better traced by high dipole molecules). Both high densities and inhomogeneous medium are common in other PDRs such as the Orion Bar (Lis & Schilke 2003). In particular, we have shown that unresolved gas components up to $n(H_2)$ $\simeq(2–6)\times10^5$ cm^{-3} are required to explain the CS J=5–4 line emission in the Horsehead. However, Abergel et al. (2003) did not find inhomogeneities in analysing ISOCAM images of the Horsehead. Nevertheless, they noted that clumpiness at scales smaller than the upper limit of the FUV penetration depth (~0.01 pc) could not be excluded. Our best models of the CS J=5–4 line emission require an unresolved component with a radius of ~5×10^{-3} pc. This component can of course be further fragmented itself. Nevertheless, it is difficult to distinguish between clumpiness at scales below ~0.01 pc and the presence of a lower density envelope surrounding the cloud. Since CO J=1–0 and 2–1 line opacities easily reach large values, their observed profiles are formed in the very outer layers of the cloud and thus they can arise from the most diffuse gas ($n(H_2)$ ~5×10^3 cm^{-3}). Interferometric observations of intermediate–J lines of high dipole species such as CS or HCO^+ will help to clarify the scenario.

The high angular resolution provided by PdBI CS and $C^{18}O$ observations reveals that the Horsehead PDR edge is characterized by steep density gradient rising from ambient densities to $n(H_2)$ ~10^5 cm^{-3} in a length of ~0.01 pc and kept roughly constant up to ~0.05 pc, where the density decreases again at least a by factor 2. The exact density values still depend on the assumed cloud depth and temperatures. In any case, the inferred *shell* of dense molecular gas has high thermal pressures ~(5–10)$\times10^6$ K cm^{-3} and this can be the signature of the processes driving the slow expansion of the PDR. Therefore, the most shielded clumps undergo effective line cooling and the regions of lower density should be compressed due to their lower internal pressure. Recent hydrodynamical simulations of the expansion of ionization and dissociation fronts around massive stars also predict that a high density molecular *shell* (10–100 times the ambient density) will be swept up behind the ionization front (Hosokawa & Inutsuka 2005 a&b). The density, pressure and temperature profiles and values predicted by these simulations at ~0.5 Myr (the Horsehead formation timescale derived from its velocity gradients by Pound et al. 2003 and Hily-Blant et al. 2005) qualitatively reproduce the values inferred from our molecular line observations and modeling. Hence, a shock front driven by the expansion of the ionized gas is probably compressing the cloud edge to the high densities observationally inferred in this work. Specific hydrodynamical simulations for the particular source physical conditions and comparison with observations will be appreciated. As noted by Hosokawa & Inutsuka (2005), the dynamical expansion of a HII region, PDR and molecular *shell* in a cloud with a density gradient

has not been studied well. We suggest the Horsehead PDR as a good target.

6.2. Temperatures

Molecular excitation, radiative transfer and chemical models are used to derive realistic abundances. The gas temperature impacts many aspects of these computations (e.g. chemical reaction rates and collisional excitation), and thus, the density and abundance uncertainties also reflects our incomplete knowledge of the thermal structure. The problem is not straightforward, since a steep temperature gradient is also expected in PDRs, and also because the most appropriate tracers of the warm gas lie at higher frequencies. The Horsehead PDR may not be an extreme case, since its FUV radiation field is not very high and photoelectric heating alone will not heat the gas to high temperatures as long as the gas is FUV–shielded. Nevertheless, our thermal balance calculations quickly lead to $T_k \simeq 10$ K. According to observations, this temperature is too low, especially in the first $\delta x \sim 30''$ representing the PDR edge. In this work we have (observationally) adopted T_k=30 K as the minimum gas temperature in our PDR calculations. In forthcoming works we will concentrate on the thermal structure of the PDR. Here we only note that either the cooling is not so effective and/or extra heating mechanisms need to be considered. The cosmic ray ionization rate was also increased by a factor $\sim$5 but it only modifies the gas temperature by $\Delta T_k \sim 4$ K.

Under these circumstances we have to conclude that the gas, or at least a fraction of it, is likely to be warmer than predicted. We note that this problem is not new. Again, high–J ^{13}CO and NH_3 observations have previously probed the existence of warm gas ($\sim$150 K) in regions where standard heating mechanisms fail to predict those values (Graf et al. 1990; Batrla & Wilson 2003). More recently, Falgarone et al. (2005) reported ISO observations of H_2 in the lowest five pure rotational lines S(4) to S(0) (8 μm to 28 μm) toward diffuse ISM gas. The observed S(1)/S(0) and S(2)/S(0) line ratios are too large to be compatible with the PDR models. These authors suggested that MHD shocks (Flower & Pineau des Forets 1998) or magnetized vortices, which are natural dissipative structures of the intermittent dissipation of turbulence (Joulain et al 1998), locally heat the gas at temperatures up to $\approx$ 1000 K. These structures add two heating sources: *i)* viscous heating through large velocity shear localized in tiny regions and *ii)* ion-neutral drift heating due to the presence of magnetic fields (ambipolar diffusion). As shown by Falgarone et al (2006), these dissipative structures are also able to trigger a hot chemistry, that is not accessible to models that do not take into account the gas dynamics. These results suggest that additional mechanical heating processes are at work. We propose that the shock waves driven by the expansion of the HII region and PDR compress the molecular gas in the cloud edge and provide it with an additional heating source.

6.3. CS and HCS^+ chemistry

According to the last (but not least) molecular data affecting CS chemistry and excitation, the mean CS abundance in the Horsehead PDR, $\chi(CS)=(7\pm3)\times10^{-9}$, implies a gas sulfur abundance of S/H $\sim(3.5\pm1.5)\times10^{-6}$, only a factor $\lesssim$4 smaller than the solar value (Asplund et al. 2005). Even lower sulfur depletion values are possible if the gas is significantly warmer than 30 K. Thus, the gas phase sulfur abundance is very close to the undepleted value observed in the diffuse ISM and not to the depleted value invoked in dense molecular clouds (e.g. Millar & Herbst 1990). However, the observed CS/HCS^+ $\simeq$175 abundance ratio can only be reproduced by photochemical models by considering the HCS^+ peak abundance, otherwise, larger ratios ($\sim10^3$) are predicted. Therefore, either the observed HCS^+ only traces the surface of the cloud where its abundance peaks, or chemical models underestimate the HCS^+ production rate. In any case, the predicted CS/HCS^+ abundance ratio scales with the gas phase sulfur abundance. The largest ratios are expected at the lowest sulfur depletions. However, the observed CS/HCS^+ $\sim$10 ratio in the diffuse ISM (Lucas & Listz 2002) is even lower than in the Horsehead. Thus, we have to conclude that present chemical models still fail to reproduce the observed CS/HCS^+ abundance ratio, at least in the stationary regime. Time–dependent photochemical computations may also help to understand the dynamical expansion of the dissociation front and the evolving molecular abundances. Besides, Gerin et al. (1997) noted that larger HCS^+ abundances are expected if the gas is in a high ionization phase. We have computed that if the cosmic ray ionization rate is increased by a factor of $\sim$5, the predicted HCS^+ abundance inside the cloud (A_V=10 mag) interestingly matches our inferred value and the CS/HCS^+ abundance ratio gets much closer to the observed ratio without the need of taking the HCS^+ abundance peak.

For the physical and FUV illuminating conditions prevailing in the Horsehead PDR, most of the gas phase sulfur is locked in S^+ for $A_V \lesssim 2$ mag and $\chi(HCS^+)$ reaches its maximum value. Besides, the derived gas phase sulfur abundance is large enough to keep $\chi(e^-)>10^{-7}$ for $A_V \lesssim 3.5$ mag. HCS^+ and S II recombination lines trace the skin of molecular clouds where S^+ is still the dominant form of sulfur. In the scenario proposed by Ruffle et al. (1999), these S^+ layers will be responsible of the sulfur depletion due to more efficient sticking collisions on negatively charged dust grains than in the case of neutral atoms such as oxygen. Even in these regions, still dominated by photodissociation, CS and HCS^+ abundances are quickly enhanced compared to other sulfur molecules. In fact, we predict that CS is the most abundant S–bearing molecule in the external layers where S^+ is still more abundant than neutral sulfur. These results are consistent with our PdBI detection of CS close to the PDR edge and show that CS is a PDR tracer. These findings are consistent with observations of S–bearing species in the diffuse ISM where CS is more abundant than SO_2, H_2S and SO (Lucas & Listz 2002).

Between $A_V \sim 2$ and $\sim$8 mag the S^+ abundance smoothly decreases. Since S^+ is a good source of electrons, the electronic fractionation also decreases accordingly. HCS^+, and thus CS, present an abundance minimum in these layers. Neutral atomic

sulfur is now the most abundant S–bearing species. Therefore, observations of the [S I]25 μm fine structure line will basically trace these intermediate layers of gas where S–bearing molecules have not reached their abundance peak. However, the exctitation energy of the [S I]25 μm line (the upper level energy is ∼570 K) is too high compared to the thermal energy available in the regions where the neutral sulfur abundance peaks ($T_k \simeq$30 K) and no detectable emission is expected. In fact, no Spitzer/IRS line detection has been reported in the Horsehead (L. Verstraete, private com.). However, since most of the neutral atomic sulfur will remain in the ground–state, the presence of a background IR source (e.g. in face–on PDRs) may allow, with enough spectral resolution and continuum sensitivity, the detection of the [S I]25 μm line in absorption.

On the other hand, sulfur in diffuse ionized gas outside the molecular cloud is in the form of sulfur ions. Mid–IR [S III] fine structure lines have been detected around the Horsehead with IRS/Spitzer (L. Verstraete, private com.). In the shielded gas, sulfur is mostly locked in S–bearing molecules together with a smaller fraction in atomic form. Our models predict that species such as SO will be particularly abundant. Jansen et al. (1995) also noted that the low gas phase sulfur abundance needed to explain the CS abundance in the Orion Bar PDR was incompatible with the observed high H_2S/CS∼0.5 abundance ratio. Therefore, a complete understanding of the sulfur chemistry will only be achieved when all the major sulfur molecules can be explained. In a forthcoming paper we analyse the photochemistry, excitation and radiative transfer of several S-bearing molecules detected by us in the Horsehead PDR.

7. Summary and Conclusion

We have presented interferometric maps of the Horsehead PDR in the CS J=2–1 line at a 3.65″×3.34″ resolution together with single–dish observations of several rotational lines of CS, $C^{34}S$ and HCS^+. We have studied the CS photochemistry, excitation and radiative transfer using the latest HCS^+ and OCS^+ dissociative recombination rates (Montaigne et al. 2005) and CS collisional cross–sections (Lique et al. 2006). The main conclusions of this work are as follows:

1. CS and $C^{34}S$ rotational line emission reveals mean densities around $n(H_2)$=(0.5–1.0)×10^5 cm^{-3}. The CS J=5–4 lines show narrower line widths than the low–J CS lines and require higher density gas components, ∼(2–6)×10^5 cm^{-3}, not resolved by a ∼10″ beam. These values are larger than previous estimates based on CO observations. It is likely that clumpiness at scales below ∼0.01 pc and/or a low density envelope play a role in the CS line profile formation.
2. Nonlocal, non–LTE radiative transfer models of optically thick CS lines and optically thin $C^{34}S$ lines provide an accurate determination of the CS abundance, $\chi(CS)$=(7±3)×10^{-9}. We show that radiative transfer and opacity effects play a role in the resulting CS line profiles but not in $C^{34}S$ lines. Assuming the same physical conditions for the HCS^+ molecular ion, we find $\chi(HCS^+)$=(4±2)×10^{-11}.
3. According to photochemical models, the gas phase sulfur abundance required to reproduce these CS and HCS^+ abundances is S/H=(3.5±1.5)×10^{-6}, only a factor ∼4 less abundant than the solar elemental abundance. Larger sulfur abundances are possible if the gas is significantly warmer. Thus, the sulfur abundance in the PDR is very close to the undepleted value observed in the diffuse ISM. The predicted CS/HCS^+ abundance ratio is close to the observed value of ∼175, especially if predicted HCS^+ peak abundances are considered. If not, the HCS^+ production is underestimated unless the gas is in a higher ionization phase, e.g. if the cosmic ray ionization rate is increased by ∼5.
4. High angular resolution PdBI maps reveal that the CS emission does not follow the same morphology shown by the small hydrocarbons emission the PDR edge. In combination with previous PdBI $C^{18}O$ observations we have modeled the PDR edge and confirmed that a steep density gradient is needed to reproduce CS and $C^{18}O$ observations. The resulting density profile qualitatively agrees to that predicted in numerical simulations of a shock front compressing the PDR edge to high densities, $n(H_2)\simeq 10^5$ cm^{-3}, and high thermal pressures, ≃(5–10)×10^6 K cm^{-3}.
5. Conventional PDR heating and cooling mechanisms fail to reproduce the temperature of the warm gas observed in the region by at least a factor ∼2. Additional mechanical heating mechanisms associated with the gas dynamics may be needed to account for the warm gas. The thermal structure of the PDR edge is still not fully constrained from observations. This fact adds uncertainty to the abundances predicted by photochemical models.

We have shown that many physical and chemical variations in the PDR edge occur at small angular scales. In addition, the molecular inventory as a function of the distance from the illuminating source can only be obtained from millimeter interferometric observations. High angular resolution observations contain detailed information about density, temperature, abundance and structure of the cloud, but only detailed radiative transfer and photochemical models for each given source are able to extract the information. A minimum description of the source geometry is usually needed. Future observations with ALMA will allow us to characterize in much more details many energetic surfaces such as PDRs.

Acknowledgements. We are grateful to the IRAM staff at Plateau de Bure, Grenoble and Pico Veleta for the remote observing capabilities and competent help with the observations and data reduction. We also thank BASECOL, for the quality of data and information provided, and F. Lique for sending us the CS collisional rates prior to publication. JRG thanks J. Cernicharo, F. Daniel and I. Jiménez-Serra for fruitful discussions. We finally thank John Black, our referee, for useful and encouraging comments. JRG was supported by the french *Direction de la Recherche* and by a *Marie Curie Intra-European Individual Fellowship* within the 6th European Community Framework Programme, contract MEIF-CT-2005-515340.

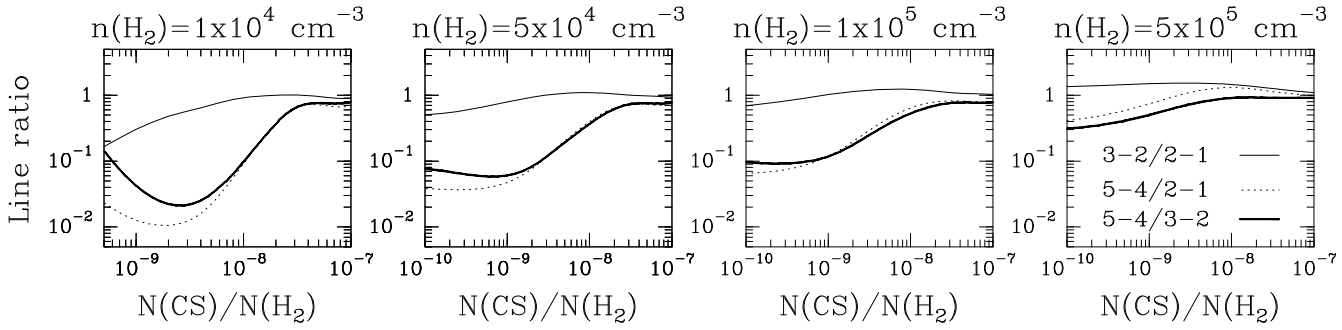

Fig. 6. Grid of CS single–component models assuming T_k= 30 K and a fixed extinction of 20 mag. Panels show different line ratios as a function of $\chi(CS)$. Each panel correspond to a single density, from $n(H_2)$=10^4 to 5×10^5 cm^{-3}. Mean observed ratios are $\frac{3-2}{2-1}\simeq$0.7, $\frac{5-4}{2-1}\simeq$0.2 and $\frac{5-4}{3-2}\simeq$0.3.

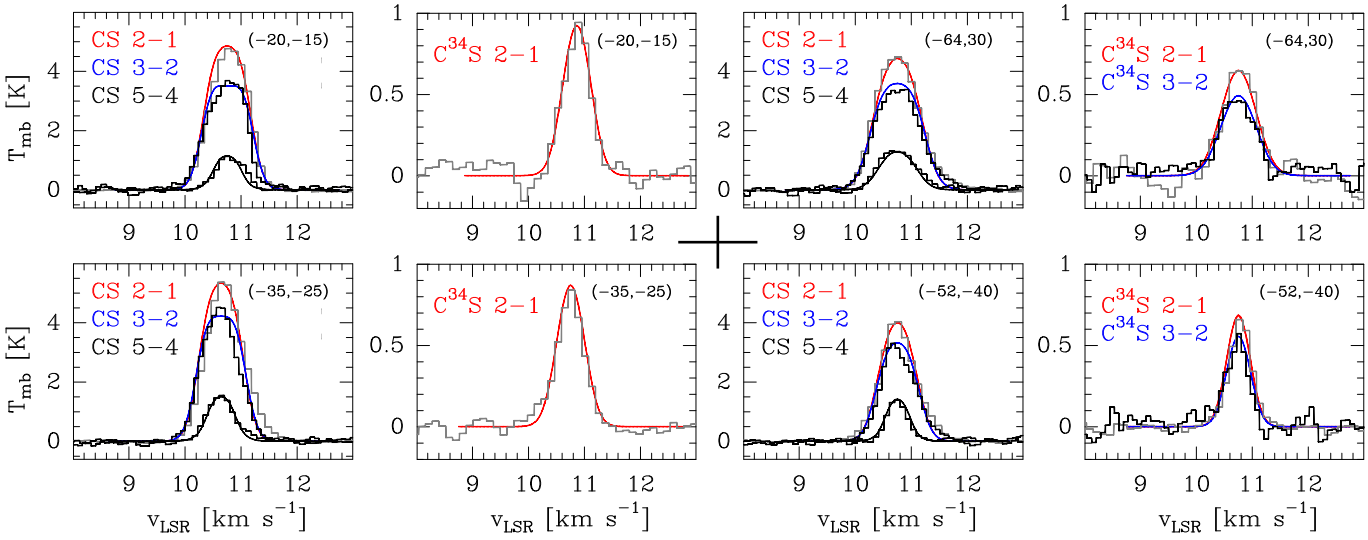

Fig. 7. Radiative transfer models for CS and $C^{34}S$ discussed in the text (curves) that best fits the IRAM–30m observations (histograms). Offsets in arcsec refer to the (0,0) position of the $C^{18}O$(2–1) map (see Fig.4). Predicted line profiles have been convolved with the telescope angular resolution at each frequency. Intensity scale is in main beam temperature.

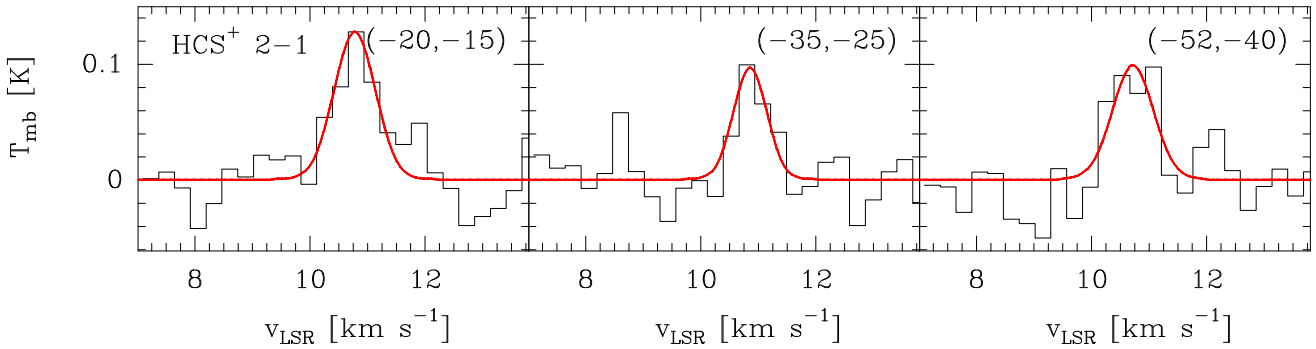

Fig. 8. IRAM–30m HCS^+(2–1) single–dish observations (histograms) at different positions of the Horsehead. Offsets in arcsec refer to the (0,0) position of the $C^{18}O$(2–1) map (see Fig.4) Radiative transfer models for HCS^+ at selected positions are also shown (curves). Predicted line profiles have been convolved with the telescope angular resolution at each frequency. Intensity scale is in main beam temperature.

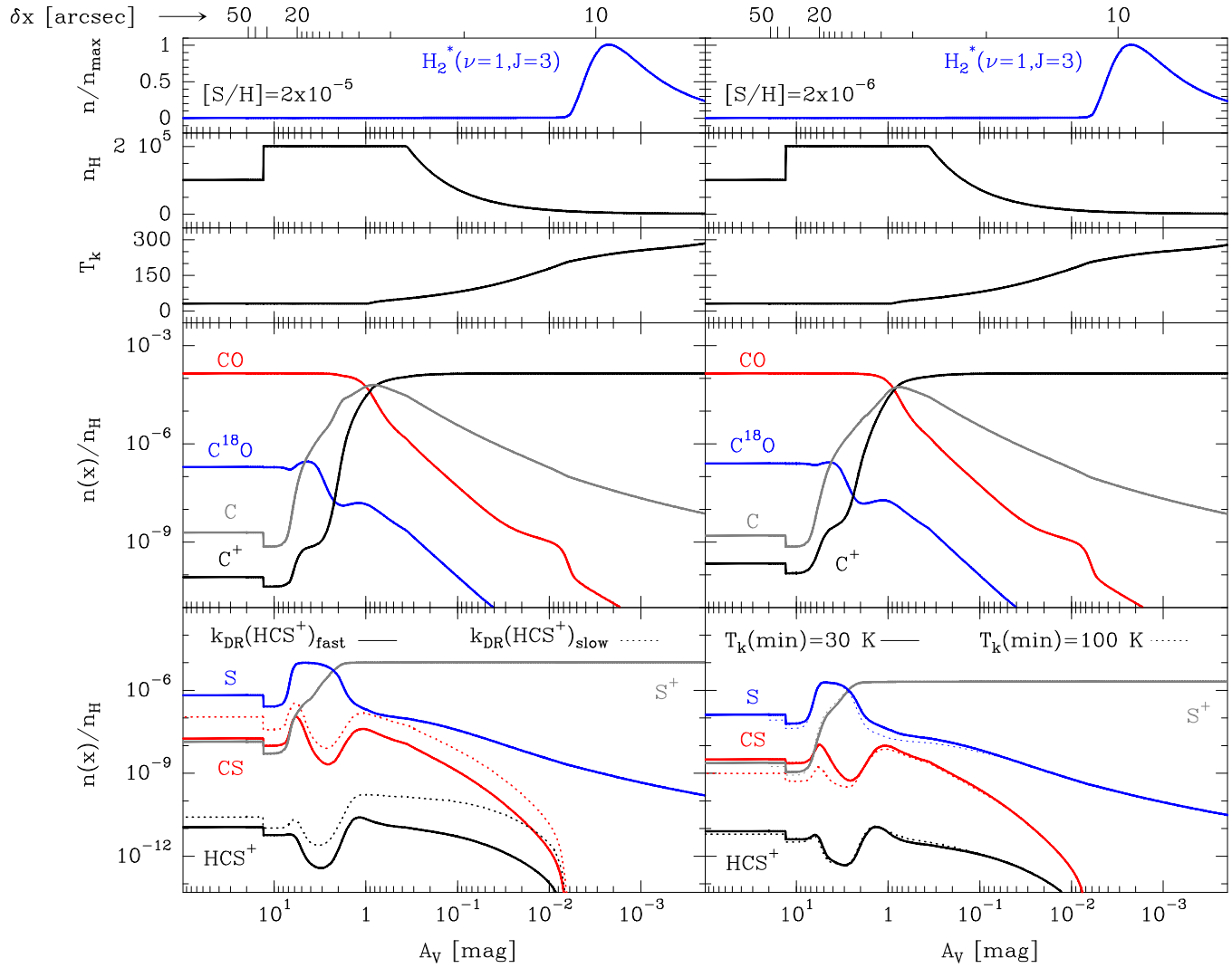

Fig. 9. Photochemical models using a unidimensional PDR code for two different sulfur gas phase abundances, (S/H=2×10^{-5}; *left*) and the minimum value found for the Horsehead (S/H=2×10^{-6}; *right*). The predicted normalized population of the H_2 v=1, J=3 level is shown in the *upper* panel and is used to place the δx–axis origin for the models. The peak of this curve is placed at the maximum of the observed H_2 1–0 S(1) 2.12 μm line emission (δx∼10″; Habart et al. 2005). Next panel shows the density profile (n_H = $n(H)$ + 2$n(H_2)$ in cm^{-3}) used in the PDR calculations that better fits the CS and C^{18}O IRAM-PdBI observations. Next panel shows the gas temperature (in K) consistently computed in thermal balance until reaches a minimum value of 30 K. *Lower* panels show the spatial variation of C^{18}O/CO/C/C$^+$ and CS/HCS$^+$/S/S$^+$ abundances (relative to n_H) across the PDR. The far–UV radiation field is χ=60 times the Draine field. Chemical rates are those of the *Ohio State University (osu)* gas–phase chemical network (September 2005 release) plus several modifications (see text). *Bottom left* panel shows the effect of using the older rate and branching ratios for the HCS$^+$ dissociative recombination on the CS and HCS$^+$ abundances (dashed curves). *Bottom right* panel shows the effect of using a minimum gas temperature of 100 K in the chemistry. Lower CS abundances and thus larger S/H values are possible as the temperature increases (dashed curves).

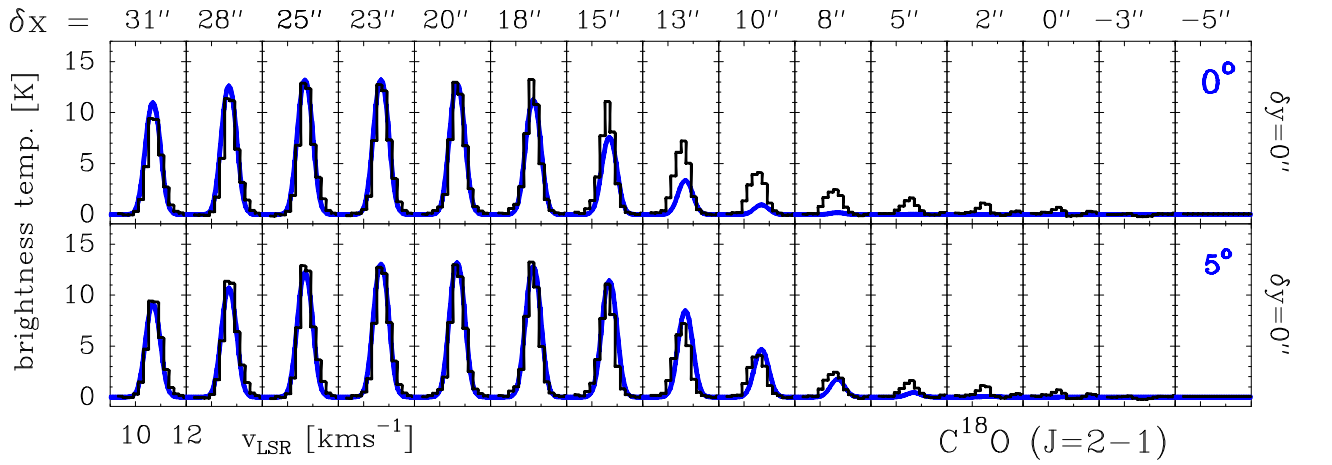

Fig. 10. IRAM-PdBI $C^{18}O$ J=2–1 spectra along the direction of the exciting star at $\delta y = 0''$ (histograms). Radiative transfer models using the output of PDR models for $C^{18}O$ (blue curve) for a density gradient and physical conditions discussed in the text. *Lower panel* shows inclination effects assuming that the PDR is inclined relative to the line of sight by a φ=5^o angle. Modeled line profiles have been convolved with an appropriate gaussian beam corresponding to each synthesized beam. Intensity scale is in brightness temperature and abscissa in LSR velocity.

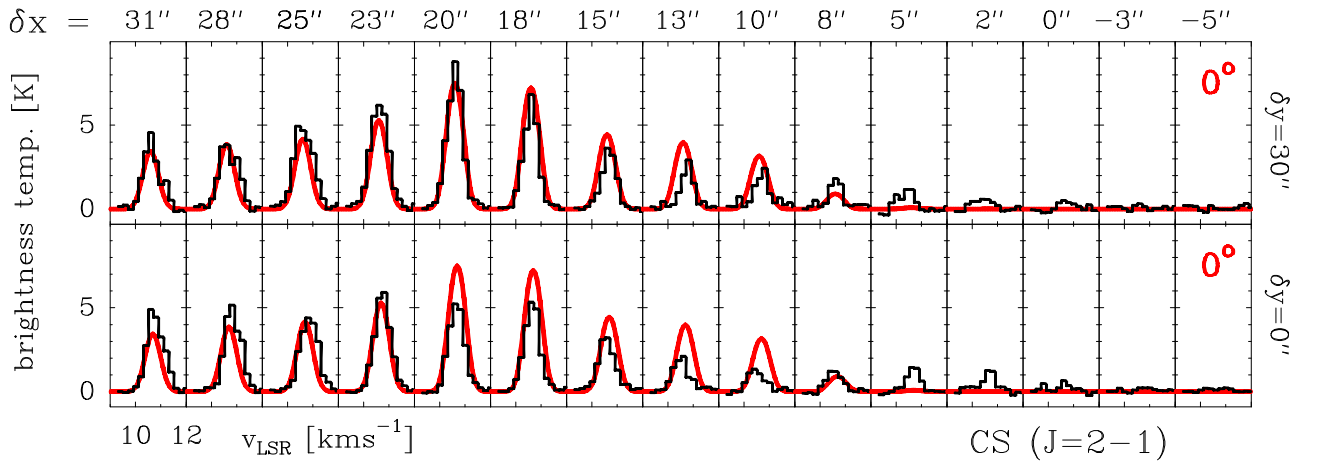

Fig. 11. IRAM-PdBI CS J=2–1 spectra along the direction of the exciting star at $\delta y = 30''$ (*upperpanel*) and $\delta y = 0''$ (*lowerpanel*). Radiative transfer models using the output of PDR models for CS (red curve) for a density gradient and physical conditions discussed in the text (assuming that the PDR is not inclined relative to the line of sight). Modeled line profiles have been convolved with an appropriate gaussian beam corresponding to each synthesized beam. Intensity scale is in brightness temperature and abscissa in LSR velocity.

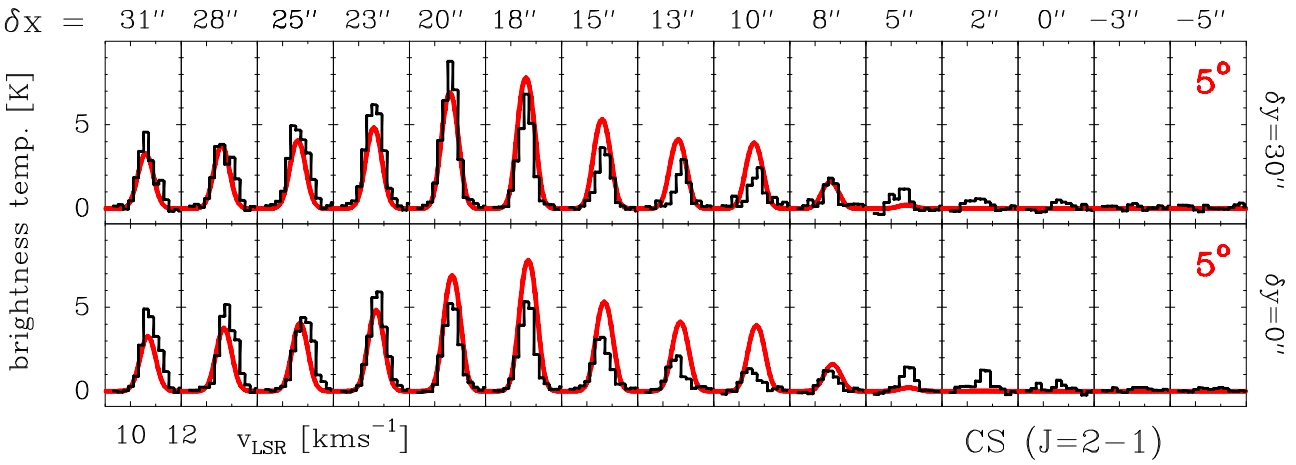

Fig. 12. IRAM-PdBI CS J=2–1 spectra along the direction of the exciting star at $\delta y = 30''$ (*upperpanel*) and $\delta y = 0''$ (*lowerpanel*). Radiative transfer models using the output of PDR models for CS (red curve) for a density gradient and physical conditions discussed in the text (assuming that the PDR is inclined relative to the line of sight by a φ=5^o angle). Modeled line profiles have been convolved with an appropriate gaussian beam corresponding to each synthesized beam. Intensity scale is in brightness temperature and abscissa in LSR velocity.

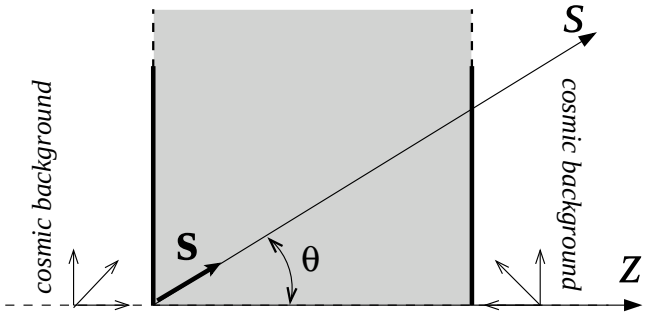

Fig. A.1. Plane–parallel geometry for a cloud isotropically illuminated by the cosmic microwave background at both surfaces.

Appendix A: Nonlocal, non–LTE radiative transfer

Radiative transfer in a medium dominated by gas phase molecules and dust grains requires the solution of the radiative transport (RT) equation for the radiation field together with the equations governing the relative level populations of the considered species. In the case of rotational line emission (far–IR to mm domain), scattering from dust grains can be usually neglected from the RT equation and steady state statistical equilibrium can be assumed for molecular populations. However, physical conditions in ISM clouds are such that molecular excitation is usually far from LTE. Therefore, a minimum treatment of the nonlocal coupling between line+continuum radiation and level populations is required. In this appendix we describe in more detail the simple model developed for this work.

A.1. Monte Carlo methodology for gas and dust radiative transfer in plane-parallel geometry

The Monte Carlo methodology or its modifications is a simple and widely adopted approach when one has to deal with moderately thick lines and flexibility to explore different geometries is required (see van Zadelhoff et al. 2002 and references therein). In this work, the *classical* description of the Monte Carlo approach for non–LTE line transfer (Bernes 1979) has been extended to include the dust emission/absorption and their effect on the source function. The code was originally developed in *fortran90* for spherical symmetry (Goicoechea 2003) and has been enlarged to semi–infinite plane–parallel geometry (from face– to edge-on). Thus, numerical discretization is transformed from spherical shells to slabs. The model includes illumination from the cosmic background at both surfaces.

The variation of the radiation field intensity along any photon path s is related to the emission and absorption properties of the medium (scattering neglected) through

$$\frac{dI_\nu}{ds} = j_\nu - \alpha_\nu I_\nu \tag{A.1}$$

where α_ν [cm^{-1}] and j_ν [erg s^{-1} cm^{-3} Hz^{-1} sr^{-1}] are the total (gas+dust) absorption and emissivity coefficients at a given frequency ν. The normal path to any plane–parallel slab is thus $dz = \mu\, ds$, with $\mu = cos\,\theta$ and where θ is the angle between z and s (see Fig. A.1). Equation A.1 is thus written as

$$\mu \frac{dI_\nu}{d\tau} = S_\nu - I_\nu \tag{A.2}$$

where the differential optical depth is given by gas and dust contributions, $d\tau = \alpha_\nu\, dz$, and $S_\nu = j_\nu/\alpha_\nu$ is referred to as the source function. Continuum emissivity from dust is assumed to be thermal and given by

$$j_\nu^{dust} = \alpha_\nu^{dust} B_\nu(T_d) \tag{A.3}$$

where B_ν is the Planck function at a given dust temperature, T_d, and α_ν^{dust} is computed from any of the dust mass absorption cross–sections available in the literature (e.g. Draine & Lee, 1984, Ossenkopf and Henning, 1994). For practical purposes, the dust absorption coefficient is assumed to be constant in all the passband around each line frequency. Hence, the number of dust continuum photons emitted per second in a given cell of material is $(4\pi/hc)\, j_\nu^{dust} V_m\, \Delta$v where V_m is the cell volume and Δv the considered passband in velocity units. Although the inclusion of dust almost does not affect molecular excitation in our work, it is included for consistency and for making predictions of higher frequency lines where it has larger effects.

Molecular lines occur at discrete frequencies, ν_{ij}, where i and j refer to upper and lower energy levels with n_i and n_j [cm^{-3}] populations respectively. Gas emission and absorption coefficients, as a function of velocity, are defined as

$$j_\nu^{gas} = \frac{hc}{4\pi}\, n_i\, A_{ij}\, \phi \quad ; \quad \alpha_\nu^{gas} = \frac{hc}{4\pi}\, (n_j\, B_{ji} - n_i\, B_{ij})\, \phi \tag{A.4}$$

where B_{ji}, B_{ij}, and A_{ij} are the transition probabilities, or Einstein coefficients, for absorption, and for induced and spontaneous emission respectively. We have assumed the same line Doppler profile (in velocity units) for emission and absorption

$$\phi = \frac{1}{b\,\sqrt{\pi}} \exp\left(-\frac{\mathbf{v} + \mathbf{v_f} \cdot \mathbf{s}}{b}\right)^2 \tag{A.5}$$

and thus considered Gaussian Doppler microturbulent and thermal broadening characterized by the broadening parameter $b^2 = \mathrm{v}_{turb}^2 + \mathrm{v}_{th}^2$. Note that any arbitrary velocity field $\mathbf{v_f}$ can be included. Here we take the possibility of having a velocity field normal to the slabs, i.e. $\mathbf{v_f}$=v$_f$ (z).

Generally speaking, the relative level populations of a considered molecule m are determined by collisions with other molecules, and/or by radiative effects caused by the cosmic background and/or by the dust continuum emission. The particular physical conditions, type of molecule and spectral domain will determine the dominant processes through the steady state statistical equilibrium equations

$$n_i \sum_{j \neq i} [R_{ij} + C_{ij}] = \sum_{j \neq i} n_j [R_{ji} + C_{ji}] \quad ; \quad n_{tot} = \sum_{J=1}^{rot\ levels} n_J \tag{A.6}$$

where C_{ij} and R_{ij} [s^{-1}] are the collisional and radiative transition rates between i and j levels. For the collisional rates of species m (CS, C^{34}S, C^{18}O and HCS$^+$) we have considered

$$C_{ij} = \gamma_{ij}^m\,(H_2)\; n(H_2) + \gamma_{ij}^m\,(He)\; n(He) + \gamma_{ij}^m\,(H)\; n(H) \tag{A.7}$$

where γ_{ij}^m [cm^3 s^{-1}] are the temperature dependent collisional de–excitation rate coefficients of m with collisional partners H_2 or He. If unknown, excitation rate coefficients are computed

through detailed balance. For consistency with the PDR modeling we have estimated the collisional rates with H atoms (simply by scaling from the He rates), since H may be the dominant partner in the diffuse regions. Radiative rates are

$$R_{ij} = A_{ij} + B_{ij}\bar{J}_{ij} \quad ; \quad R_{ji} = B_{ji}\bar{J}_{ji} \tag{A.8}$$

where $\bar{J}_{ij}$ is the intensity of the radiation field integrated over solid angles and over the line profile. External illumination by cosmic background, dust continuum emission and line photons from different spatial regions contribute to $\bar{J}_{ij}$. Hence, the solution of molecular excitation implicitly depends on the nonlocal radiation field, which obviously depends on level populations in many cloud points. $\bar{J}_{ij}$ is explicitly computed in the Monte Carlo approach, and thus, the RT-excitation problem is solved iteratively until desired convergence in some physical parameter (generally the level populations) is achieved. LTE level populations at a constant fictitious T_{ex} were used for the first iteration. In the case of CS modeling, T_{rot} from the observational rotational–diagrams (Fig.5) was used.

The RT problem is then simulated by the emission of a determined number of model photons (both sides external illumination, continuum and line photons) in a similar way to that originally described by Bernes (1979). Model photons represent a large quantity of *real* photons randomly distributed over the line profile A.5 and emitted at random cloud positions and directions. Each model photon is followed through the different slabs until it escapes the cloud or until the number of represented real photons become insignificant. Note that the angle θ between the photon direction and the normal to the slabs remains constant in all the photon path. In spherical geometry the θ angle between the photon direction and the radial direction changes in each photon step and thus has to be computed repeatedly. In addition, model photons sent in the $cos\,\theta \simeq 0$ direction in semi–infinite plane–parallel geometry will almost never escape the cloud. Thus, a minimum number of represented real photons is defined otherwise the photon is not followed anymore. In this way, the Monte Carlo simulation explicitly computes the induced emissions caused by the different types of model photons in all the slabs. At the end of the simulation, an averaged value for the $B_{ij}\bar{J}_{ij}$ that independently accounts for external illumination, continuum emission and line emission is stored for every slab ($\sum S_{ij,m}$ in Bernes formalism). Populations are then obtained in each slab by solving:

$$n_i \sum_{j\neq i}[A_{ij} + \sum S_{ij,m} + C_{ij}] = \sum_{j\neq i} n_j\,[\frac{g_i}{g_j}\sum S_{ij,m} + C_{ji}] \tag{A.9}$$

A reference field for all types of model photons was included to reduce the inherent random fluctuations (i.e. the variance) of any Monte Carlo simulation (see Bernes 1979, for details). When a prescribed convergence in level the populations is reached, the total (gas+dust) source function is completely determined and the emergent intensity can be easily computed by integrating Eq. A.2.

For spherical geometry, the code was successfully benchmarked against two test problems, the *Bernes' CO cloud* (Bernes 1979) and the *HCO$^+$ collapsing cloud, problem 2a* of the 1999 Leiden benchmark (van Zadelhoff et al. 2002). In the case of plane–parallel geometry, several thermalization tests for the CS excitation (without dust emission) were successfully performed. Excitation temperatures as a function of the normal coordinate to slabs z are shown for CS J=1–0, 2–1, 3–2 and 5–4 transitions in Fig. A.2. Model parameters are T_k=20 K, $n(H_2)$=10^5 cm^{-3} and χ(CS)=7×10^{-9}. Different excitation conditions are considered. Upper model: $A_{ij}/C_{ij} = 0$ and T_{ex} is correctly thermalized to T_{kin} (LTE). Middle model: collisional rates from Lique et al., (filled squares; 2006) and Turner et al. (empty circles; 1992) and resulting non–LTE excitation (see section 5.1). As noted by Lique et al., their new collisional rates produce larger excitation temperatures, especially as J increases. For the Horsehead physical conditions this implies that the estimated densities and/or abundances with Turner et al. collisional rates are ∼10% larger. Lower model: collisional excitation neglected and T_{ex} is radiatively thermalized to the cosmic background temperature at T_{bg}=2.7 K.

A.2. A model for an edge–on cloud with inclination

In order to benchmark the spatial distribution of the PDR code abundance predictions with our interferometric line observations, we now can use the simple model described above to compute the synthetic spectrum of a required molecule. To do that, the PDR code output was used as an input for the RT calculation. In particular, the density profile (both $n(H_2)$ and $n(H)$), temperature profile (both T_k and T_d) and species abundance are carefully interpolated from the PDR spatial grid output. In practice, the slab discretization for the RT calculation has to be precise enough to sample the abundance, density and temperature variations at the edge of the PDR (where most of the changes occur). In most RT computations, ∼50 slabs were judged to give satisfactory sampling of the PDR variations. For an edge–on configuration, after a Monte Carlo simulation, RT equation A.2 was integrated in a grid of different lines of sight (similar to impact parameters in spherical geometry) as

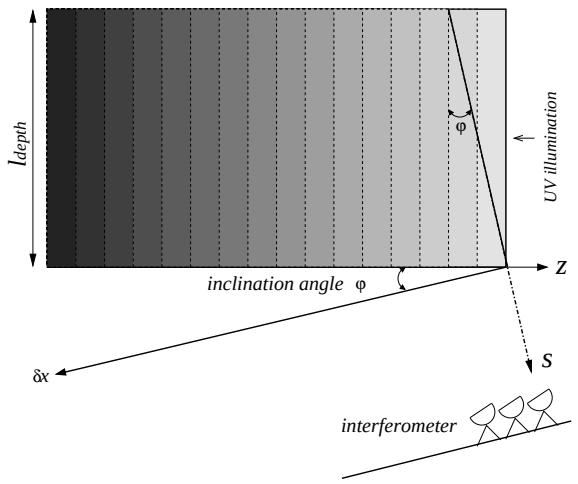

Fig. A.3. Adopted geometry for a plane-parallel PDR inclined by an small angle φ relative to the line of sight s. In this sketch, z denotes the normal direction to the slabs and also the UV illumination direction.

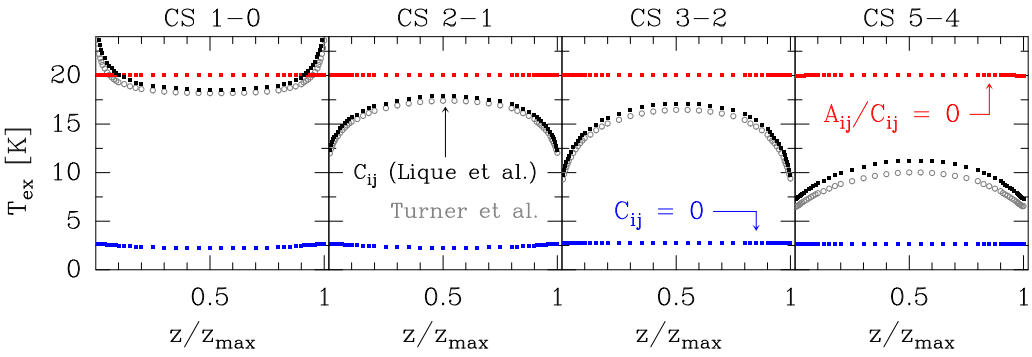

Fig. A.2. Thermalization tests for a plane-parallel cloud illuminated by the cosmic background at both surfaces (z/z_{max}=0,1).

depicted in Fig. A.3. Lines of sight can be inclined by an angle φ respect to the slabs normal ($ds = dz/sin\ \varphi$). Therefore, the maximum integration path is $l_{depth}/cos\ \varphi$ where l_{depth} is the assumed cloud spatial depth. To produce a synthetic map, results are then convolved in a grid of cloud points with an angular resolution characterized by a gaussian with hpbw equal to that of the synthesized interferometric beam.

References

Abergel, A., Bernard, J. P., Boulanger, F. et al. 2002, A&A, 389, 239.
Abergel, A. et al. 2003, A&A, 410, 577.
Anthony-Twarog, B. J. 1982, A&J, 87, 1213.
Asplund, M., Grevesse, N., & Sauval, A. J. 2005 in ASP Conf. Ser. 336, Cosmic Abundances as Records of Stellar Evolution and Nucleosynthesis, ed. F. N. Bash & T. G. Barnes, 25
Batrla, W. & Wilson, T. L. 2003, A&A, 408, 231
Bernes, C. 1979, A&A, 73, 67.
Bogey, M., Demuynck, C., & Destombes, J. L. 1981, Chem.Phys.Letters, 81, 256
Boogert, A. C. A. et al. 2000, A&A, 360, 683.
Cernicharo, J. & Guelin, M. 1987, A&A, 176, 299.
Dartois, E. 2005, Space Science Reviews, 119, Issue 1-4, p. 293-310
Draine, B. T. 1978, ApJS, 36, 595.
Draine, B. T. & Lee, H.M. 1984, ApJ, 285, 89.
Emerson, D. T., & Graeve, R. 1988, A&A, 190, 353.
Falgarone, E., Verstraete, L., Pineau Des Forets, G. & Hily-Blant, P. 2005, A&A, 433, 997.
Falgarone, E., Pineau Des Forets, G., Hily-Blant, P. & Schilke, P. 2006, A&A, in press.
Flower, D. R., & Pineau des Forets, G. 1998, MNRAS, 297, 1182.
Flower, D. R. 2001, JPhB, 34, 2731
Frerking, M. A., Wilson, R. W., Linke, R. A., & Wannier, P. G. 1980, ApJ, 240, 65.
García-Rojas, J., Esteban, C., Peimbert, M., Costado, M. T., Rodrguez, M., Peimbert, A. & Ruiz, M. T. 2006, MNRAS, 368, 253
Gerin, M. et al. 1997, A&A, 318, 579.
Gibb, E. L., Whittet, D. C. B., Boogert, A. C. A., & Tielens, A.G.G.M. 2004, ApJS, 151, 35.
Goicoechea, J.R. 2003, Ph. D. Thesis, Universidad Autonoma de Madrid, September 2003.
Goldsmith, P.F., & Langer, W.D. 1999, ApJ, 517, 209.
González-Alfonso, E. & Cernicharo, J. 1993, A&A, 279, 506.
Graedel, T. E., Langer, W. D., & Frerking, M. A. 1982, ApJS, 48, 321.
Graf, U. U., Genzel, R., Harris, A. I., Hills, R. E., Russell, A. P. G. & Stutzki, J. 1990, ApJ, 358, L49.
Gueth, F., Guilloteau, S. & Bachiller, R. 1996, A&A, 307, 891-897.
Habart, E., Abergel, A., Walmsley, C. M., Teyssier, D. & Pety, J. 2005, A&A, 437, 177-188.
Hily-Blant, P., Teyssier, D., Philipp, S. & Gusten, R. 2005, A&A, 440, 909.
Hosokawa, T. & Inutsuka S. 2005a, ApJ, 623, 917.
Hosokawa, T. & Inutsuka S. 2005b, astro-ph/0511165
Howk, J. C., Sembach, K. R., & Savage, B. D. 2006 2006, ApJ, 637, 333.
Irvine, W. M., Schloerb, F. P., Hjalmarson, A. & Herbst, E. 1985, Protostars and planets II (A86-12626 03-90). Tucson, AZ, University of Arizona Press, 1985, 579-620
Jansen, D. J., Spaans, M., Hogerheijde, M. R., & van Dishoeck, E. F. 1995, A&A, 303, 541.
Joulain, K., Falgarone, E., Pineau des Forets, G. & Flower, D. 1998, A&A, 340, 241.
Le Bourlot, J., Pineau Des Forets, G., Roueff, E., & Flower, D. R. 1993, A&A, 267, 233.
Le Petit, F., Nehmé, C, Le Bourlot, J. & Roueff, E. 2005, ApJS, preprint, doi:10.10861'503252'.
Lique, F., Spielfiedel, A. & Cernicharo, J. 2006, A&A, 451, 1125
Lis, D. C., & Schilke, P. 2003, ApJ, 597, L145.
Lucas, R., & Liszt, H. 1998, A&A, 337, 246.
Lucas, R., & Liszt, H. 2002, A&A, 384, 1054.
Martín-Hernández et al. 2002 2002, A&A, 381, 606
Martín, S., Martín-Pintado, J., Mauersberger, R., Henkel, C., & García-Burillo, S. 2005, ApJ, 620, 210
Millar, T. J. & Herbst, E. 1990, A&A, 231, 466.
Montaigne, H., Geppert, W. D., Semaniak, J., et al. 2005, ApJ, 631, 653.
Monteiro, T. 1984, MNRAS, 210, 1
Neufeld, D.A., Wolfire, M.G., & Schilke, P. 2005, ApJ, 628, 60.
Ohishi, M. & Kaifu, N. 1998, Chemistry and Physics of Molecules and Grains in Space. Faraday Discussions No. 109. The Faraday Division of the Royal Society of Chemistry, London, 1998, 205
Ossenkopf, V. & Henning, Th. 1994, A&A, 291, 943.
Palumbo, M.E., Geballe, T.R., Tielens, A.G.G.M. 1997, ApJ, 479, 839.
Pankonin, V., & Walmsley, C.M. 1978, A&A, 64, 333.
1973, ARA&A, 11, 51.
Pety, J., Teyssier, D., Fossé, D., Gerin, M., Roueff, E., Abergel, A., Habart, E. & Cernicharo, J. 2005, A&A, 435, 885-899.
Pety, J. 2005, in SF2A-2005: Semaine de l'Astrophysique Francaise, 721
Pound, M. W., Reipurth, B. & Bally, J. 2003, A&J, 125, 2108-2122.
Reipurth, B., & Bouchet, P. 1984, A&A, 137, 1.
Ruffle, D. P., Hartquist, T. W., Caselli, P. & Williams, D. A. 1999, MNRAS, 306, 691.
Tieftrunk, A., Pineau des Forets, G., Schilke, P. & Walmsley, C. M. 1994, A&A, 289, 579.

Teyssier, D., Fossé, D., Gerin, M., Pety, J., Abergel, A. & Roueff, E. 2004, A&A, 417, 135-149.
Turner, B. E., Chan, K.W, Green, S., & Lubowich, D. A. 1992, ApJ, 399, 114.
van der Tak, F.F.S., Boonman, A.M.S., Braakman, R., & van Dishoeck, E.F. 2003, A&A, 412, 133
van Dishoeck, E. F. 1988, Rate Coefficients in Astrochemistry. Editors, T.J. Millar, D.A. Williams; Publisher, Kluwer Academic Publishers, Dordrecht, Boston, 49.
van Zadelhoff, G.-J., Dullemond, C. P., van der Tak, F. F. S. et al. 2002, A&A, 395, 373.
Wakelam, V., Caselli, P., Ceccarelli, C., Herbst, E. & Castets, A. 2003, A&A, 422, 159
Wannier, P. G. 1980, ARA&A, 18, 399.
Zhou, S., Jaffe, D. T., Howe, J. E. et al. 1993, ApJ, 419, 190.